Detecting rapid lateral changes of upper mantle discontinuities using azimuth-dependent P-wave receiver functions and multimode surface waves

K. Tarumi[1,*] and K. Yoshizawa[1,2]

[1] Department of Natural History Sciences, Graduate School of Science, Hokkaido University, Sapporo 060-0810, Japan

[2]Department of Earth & Planetary Sciences, Faculty of Science, Hokkaido University, Sapporo 060-0810, Japan.

[*]Corresponding author: tarumi.kotaro.jp@gmail.com

–

Tarumi, K., & Yoshizawa, K. (2025). Detecting rapid lateral changes of upper mantle discontinuities using azimuth-dependent P-wave receiver functions and multimode surface waves. *Physics of the Earth and Planetary Interiors*, 107468. https://doi.org/10.1016/j.pepi.2025.107468

Detecting rapid lateral changes of upper mantle discontinuities using azimuth-dependent P-wave receiver functions and multimode surface waves

Kotaro Tarumi[a,b,*], Kazunori Yoshizawa[a,b]

[a]Department of Natural History Sciences, Graduate School of Science, Hokkaido University, Sapporo 060-0810, Japan., Sapporo, 060-0810, Japan
[b]Department of Earth and Planetary Sciences, Faculty of Science, Hokkaido University, Sapporo, 060-0810, Japan

---

ARTICLE INFO

Keywords:
Receiver function
Surface waves
Australia
Lithosphere-Asthenosphere Boundary
Mid-Lithospheric Discontinuity
X-Discontinuity

ABSTRACT

Lateral structural variations in the upper mantle generate azimuthal dependence in receiver functions (RFs) based on incoming directions of body waves. Although these azimuthal variations in RFs have not been considered in earlier studies of RF inversions, they provide a means to image localized changes in upper mantle interfaces. In this study, we incorporate azimuth-dependent RFs into a joint Bayesian inversion with multimode surface waves, applying this approach to major permanent broadband stations in Australia. The resulting models reveal dependence on event directions, and by identifying P-to-S conversion depths, we constructed a localized map of conversion points, reflecting local lateral variations of upper mantle discontinuities beneath each station. At the CTAO station in northeastern Australia, the lithosphere thickens rapidly northwestward, from 70 km to 120-130 km depth, corresponding to the tectonic boundary with the western cratonic region. At stations in western and central Australia, lithospheric thickness also varies laterally within the stable cratons, though these changes are more gradual than those in northeastern Australia. In addition to the lithosphere-asthenosphere boundary (LAB), both mid-lithospheric discontinuities (MLDs) and X-discontinuities (X-Ds) are observed in the local 1-D profiles. The X-Ds, characterized by seismic velocity jumps below the LAB, are found at multiple depths around 170, 220, 260, and 310 km, depending on location, accompanying the weakened radial anisotropy across these depths. The multiple MLDs are also identified in the cratonic regions, showing substantial variations in their seismological properties, including both positive or negative S-velocity jumps, which vary with location and depth. Our approach, incorporating azimuth-dependent RFs, enables the detection of localized changes in the upper mantle discontinuities and associated elastic properties, providing new insights into the complex layering of the upper mantle.

---

1. Introduction

Upper mantle discontinuities are key to understanding the evolutionary processes of the continental lithosphere and underlying asthenosphere. Seismic interfaces within the continental upper mantle are essential for clarifying the tectonic processes that long-lived continents have undergone. Although these seismic discontinuities have been extensively investigated in various seismological studies, their spatial distributions and elastic properties remain controversial, even in continental regions with extensive seismic networks (e.g., Fischer et al., 2020).

Many earlier tomography models based on surface wave data have provided valuable insights into the seismic structure of the continental upper mantle (e.g., Debayle and Kennett, 2000; Yoshizawa and Kennett, 2004; Yuan et al., 2011), revealing the thick lithosphere in continental cratons and the thinner lithosphere in younger, tectonically active regions (Fischer et al., 2020). However, surface wave approaches have intrinsic limitations in constraining upper mantle interfaces, as the long wavelengths of surface waves are insensitive to sharp velocity gradients. In contrast, teleseismic receiver functions (RFs) have been widely used to image the upper mantle discontinuities, owing to their

---

[*] Corresponding author
✉ `tarumi.kotaro.jp@gmail.com` (K. Tarumi)
ORCID(s): 0009-0002-9030-5408 (K. Tarumi); 0000-0003-2282-3748 (K. Yoshizawa)
🐦 `https://twitter.com/<@mil\protect\T1\textunderscoreglobalseis>` (K. Tarumi)

good sensitivities to impedance contrasts and their capability to identify conversions of P-to-S (Ps) or S-to-P (Sp) phases across interfaces (e.g., Rychert et al., 2005, 2007; Abt et al., 2010; Ford et al., 2010; Liu et al., 2020; Rein et al., 2020).

Recent RF studies analyzing Sp conversions have reported enigmatic interfaces beneath continental cratons, associated with sharp S-wave speed reductions above the Lithosphere-Asthenosphere Boundary (LAB), known as the Mid-Lithospheric Discontinuity (MLD) (Fischer et al., 2010, 2020). Like the LAB, the MLD is key to unraveling ancient tectonic history preserved within the cratonic lithosphere. Moreover, other seismological studies have suggested the existence of an enigmatic X-discontinuity (or considered as the Lehmann discontinuity) beneath the LAB (Rein et al., 2020; Srinu et al., 2021; Pugh et al., 2021). However, unlike surface waves, RFs cannot directly constrain 3-D seismic velocity structures, leaving the spatial distribution and elastic properties of upper mantle discontinuities a subject of ongoing debate.

1.1. Recent receiver function inversions

Over the past few decades, numerous studies have combined surface wave dispersion (SWD) data with teleseismic RFs to overcome the inherent limitations of surface-wave and body-wave analyses (Julià et al., 2000; Vinnik et al., 2005; Bodin et al., 2012; Tkalčić et al., 2011; Bodin et al., 2014; Calò et al., 2016; Kim et al., 2016; Taira and Yoshizawa, 2020; Ai et al., 2023). Recent joint inversion studies have utilized hierarchical trans-dimensional Bayesian inference to estimate seismic wave speed structures, including the depths of upper mantle discontinuities (e.g., Bodin et al., 2012, 2014; Kim et al., 2016; Taira and Yoshizawa, 2020; Ai et al., 2023). However, this widely used joint inversion approach encounters challenges in imaging deep upper mantle discontinuities (e.g., LAB, X-Ds) due to the limited sensitivity of fundamental-mode SWD data and the limitations of stacked RFs, which can be affected by moveout effects and azimuthal variations in individual RFs.

Although SWDs enable us to constrain the absolute seismic shear velocity, the exclusive use of the fundamental modes limits the imaging of deeper structures below 200 km. The sensitivity of the fundamental mode SWDs diminishes significantly at greater depths, especially for Love wave (Figure S1). In contrast, surface wave overtones become sensitive to deeper structures, enabling better resolution throughout the entire upper mantle (e.g., Yoshizawa and Kennett, 2004; Yoshizawa and Ekström, 2010; Xu and Beghein, 2019). However, since multimode phase speed measurements are not straightforward, several earlier studies employed only fundamental-mode SWDs (e.g., Calò et al., 2016). To enhance vertical resolution, Taira and Yoshizawa (2020) incorporated multimode SWDs into joint inversions with the P-wave RFs (P-RFs).

While RF inversions typically rely on stacked RFs derived from numerous individual RFs from many events, this approach presents two major difficulties due to intrinsic issues in the stacking process: the dependence of RF data on the range of epicentral distances and the back-azimuth of seismic events. The first issue is related to the moveout effect arisen from dependence on the distance range. This effect results in relative travel time differences between a parent phase (P-wave for P-RFs; S-wave for S-RFs) and the daughter phases (S for P-RFs; P for S-RFs), which vary with epicentral distance (or the slowness) (e.g., Kind and Yuan, 2011). To address this issue, conventional RF inversion studies have often limited the range of epicentral distances (e.g., Bodin et al., 2014; Calò et al., 2016; Taira and Yoshizawa, 2020). The second issue is the azimuthal dependence of RFs on the incoming direction of teleseismic parent waves, which results from lateral variations in seismic structure and the presence of layered anisotropic media with a horizontal symmetry axis (i.e., the azimuthal anisotropy) (Levin and Park, 1997; Frederiksen and Bostock, 2000; Frederiksen et al., 2003; Tonegawa et al., 2005; Nagaya et al., 2008; Kumar et al., 2011; Park and Levin, 2016).

These issues are generally neglected in many RF studies that employ either time-to-depth migration or inversions for velocity profiles (e.g., Rychert et al., 2005; Abt et al., 2010; Ford et al., 2010; Bodin et al., 2014; Taira and Yoshizawa, 2020; Birkey et al., 2021). However, such azimuth-dependent RFs have proven useful for imaging laterally heterogeneous structures through common conversion point (CCP) stacking, both in subduction zones (e.g., Tonegawa et al., 2005; Gilbert et al., 2006; Shi et al., 2015; Cheng et al., 2017; Kim et al., 2021) and continental regions (e.g. Kind et al., 2012; Sippl, 2016; Kennett and Sippl, 2018; Kind et al., 2020)). Although CCP stacking can yield clear structural images, it requires a dense station distribution, which is not always available in target research areas. Azimuth-dependent RFs have also been used to map crustal and mantle azimuthal anisotropy (Shiomi and Park, 2008; Nagaya et al., 2008; Bianchi et al., 2010; Nagaya et al., 2011; Ford et al., 2016; Chen et al., 2021). Bodin et al. (2016) pioneered the use of azimuth-dependent P-RFs in the trans-dimensional inversion to estimate azimuthal anisotropy beneath a station. However, no studies have yet attempted to image lateral variations in seismic interfaces through inversion.

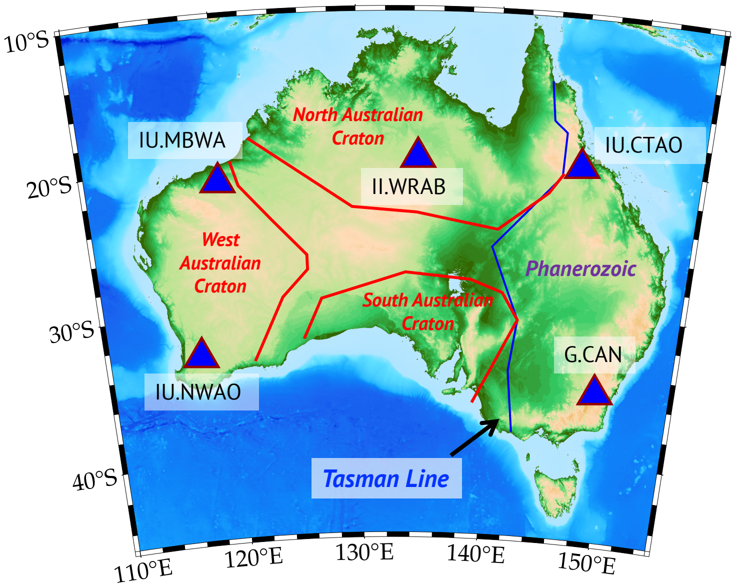

Figure 1: Map of the study region showing the locations of employed permanent stations (triangles). Red lines represent the cratonic margins of the North Australian Craton (NAC), South Australian Craton (SAC), and West Australian Craton (WAC). The blue line delineates the Tasman Line, the surface geological boundary separating cratonic regions in central and western Australia from the Phanerozoic basement in eastern Australia.

Calò et al. (2016) employed the azimuth-dependent dataset of P-RFs to examine differences in inversion results. Although they observed variations in the estimated shear wave velocity profiles and discontinuity depths, these azimuthal effects were not fully considered. If rapid changes in discontinuity depth exist beneath a station, performing multiple inversions with RF datasets from different azimuth groups could capture such localized variations, potentially offering deeper insights into seismic interfaces, even from a single station.

1.2. Australian tectonics and the scope of this paper

The Australian continent is the fastest-moving continental plate, drifting at about 6–7 cm/year (Argus et al., 2011), which was formed through ancient collisions of three major cratons - the West Australian Craton (WAC), the North Australian Craton (NAC), and the South Australian Cratons (SAC) - during the Proterozoic era (1.3–1.0 Ga) (e.g., Myers et al., 1996; Yoshida and Yoshizawa, 2020). The present-day continent comprises cratonic regions in central and western Australia and the eastern province formed by the Phanerozoic orogeny (Figure 1). Previous three-dimensional shear wave speed models from surface-wave tomography (e.g., Fishwick et al., 2008; Kennett et al., 2013; Yoshizawa, 2014; Magrini et al., 2023) have revealed the large-scale lithosphere-asthenosphere system beneath the Australian continent. The Australian LAB is relatively flat across the cratonic zones but rapidly deepens westward in Phanerozoic eastern Australia (e.g., Kennett et al., 2013; Yoshizawa, 2014; Davies et al., 2015; Magrini et al., 2023). Based on multimode surface-wave tomography, Fishwick et al. (2008) proposed a stepwise lithospheric change from east (100 km) to west (100–150 km), potentially inducing strong azimuthal dependencies in P-RFs.

In this study, we aim to estimate localized variations in the depths of upper mantle discontinuities using azimuth-dependent P-RFs. We incorporated azimuth-dependent P-RFs into the joint Bayesian inversion with multimode SWDs (Taira and Yoshizawa, 2020) and applied this approach to five long-standing permanent stations in the Australian continent (Figure 1). We then compiled multiple inversion results to map Ps conversion depths around each station, revealing new insights into Australian upper mantle discontinuities. Our key findings on the MLDs and X-Ds provide valuable clues to understanding the spatial distribution and physical properties of these interfaces.

Mode	Rayleigh	Love
Fundamental	30 – 200 s	30 – 200 s
1st	35 – 170 s	33 – 170 s
2nd	55 – 150 s	60 – 125 s
3rd	45 – 90 s	50 – 95 s
4th	35 – 65 s	45 – 70 s

Table 1
Period ranges of surface wave dispersion data. Ordinal numbers indicate overtones.

2. Data sets

Here, we summarize our data sets of multimode phase speeds of Rayleigh and Love waves (surface wave dispersions: SWDs) and P-to-S receiver functions (P-RFs), which are used in the joint inversion analyses described in the following section.

2.1. Multi-mode surface-wave dispersion

Our SWD dataset is based on the phase speed maps constructed by Yoshizawa (2014), as used by Taira and Yoshizawa (2020). This dataset from Yoshizawa (2014) comprises regional-scale multi-mode phase speed maps that cover Australia and surrounding regions.

Yoshizawa (2014) initially performed non-linear waveform fitting to measure path-averaged multimode phase speeds ray path. This method, originating with Yoshizawa and Kennett (2002b), was further refined with empirical criteria to automatically extract the multi-mode dispersion data (Yoshizawa and Ekström, 2010). Although overtone phase speed measurements are challenging due to the overlap of multiple modes, the fully nonlinear waveform fitting approach effectively extracts phase speed information for multimode surface waves (Yoshizawa and Kennett, 2002b; Yoshizawa and Ekström, 2010; Xu and Beghein, 2019). This method has also been applied to seismic records from Mars (Xu et al., 2021) and ambient noise tomography (Takagi and Nishida, 2022). In the second step, Yoshizawa (2014) performed 2-D mapping of the measured multimode phase speeds, incorporating the finite-frequency effects on seismic surface waves using the influence zone concept from Yoshizawa and Kennett (2002a). Including finite-frequency effects accounts for lateral heterogeneities around the great-circle path between a source and a receiver, resulting in a high-quality multimode SWD database.

From these multimode phase velocity maps, we extract localized dispersion curves at each station. Extracted phase speed dispersion diagrams are shown in Figure S2. Surface wave overtones are sensitive to structures below 200 km depth (Figure S1), while the fundamental mode sensitivity is limited to shallower depths (< 200km), particularly with the rapid decay of the sensitivity kernel for the fundamental Love wave. This limited sensitivity results in reduced resolution of SH wave speed or radial anisotropy structures. Taira and Yoshizawa (2020) demonstrated that higher-mode dispersion curves enhanced the vertical resolution of radially anisotropic structures. Following previous research, we use phase speed dispersion data from the fundamental up to the 4th higher mode. The period ranges for each mode of Rayleigh and Love waves used in this study are summarized in Table 1.

2.2. Azimuth-dependent P-wave receiver functions for permanent stations

We used three-component broadband seismograms, rotating the two horizontal components into radial and transverse components. P-RFs were estimated by deconvolving the vertical component from the radial component (Langston, 1979). While our waveform processing generally follows Taira and Yoshizawa (2020), we made minor updates to the deconvolution method and treatment of azimuthal dependencies in P-RFs. To accurately handle azimuth-dependent P-RFs, we made collections of horizontal misorientations of each station using our station orientation catalog (Tarumi and Yoshizawa, 2025), available through the Zenodo repository (Tarumi and Yoshizawa, 2024).

For waveform processing, we selected events with moment magnitudes between 5.5 and 7.5, normalized P-wave radiation above |0.5| (from the Global CMT catalog; Dziewonski et al., 1981; Ekström et al., 2012), epicentral distances between 30 and 90 degrees, and event depths less than 300 km. Seismograms were bandpass-filtered in two frequency ranges (0.03–0.2 Hz and 0.03-0.5 Hz). We discarded low-quality waveforms with S/N ratios below 5 on the vertical component and below 3 on the radial component. In this study, we followed Taira and Yoshizawa (2020) to set the noise window as 80–20 s before the P-wave onset. We then deconvolved the vertical component from the radial component of the observed seismograms using a modified version of the extended-time multi-taper (EXMT) receiver function technique (Shibutani et al., 2008). In the spectral division step, we applied a flat-level damping factor equal to 0.1 % of the maximum vertical auto-spectral amplitude, instead of the noise-based damping term used in the original EXMT formulation by Shibutani et al. (2008). A brief explanation of the formulation is provided in the Supplementary Material (Text S1).

Conventional RF inversion studies, particularly in continental regions, generally stack large amounts of P-RF data while restricting events in a limited range of epicentral distance and/or back-azimuth (e.g., Julià et al., 2000; Bodin et al., 2012; Vinnik et al., 2014; Kim et al., 2016; Calò et al., 2016; Taira and Yoshizawa, 2020; Akuhara et al., 2021). The stacked RF is often treated as an averaged P-RF, representing a 1-D stratified structure around the station and neglecting azimuthal variations due to the incoming direction of P-waves. However, P-RFs are sensitive to the back-azimuth of events, as they reflect lateral structural changes or anisotropic layering around the station (e.g., Tonegawa et al., 2005; Kumar et al., 2011). Teleseismic P-waves are converted to S-waves when transversing structural boundaries, so rapid lateral variations in seismic structure beneath a station induce significant back-azimuthal dependencies in P-RFs on the incoming P-wave direction (e.g., Figure 3 (b)). These azimuthal dependencies in RFs, which have been neglected in earlier studies (e.g., Taira and Yoshizawa, 2020), can be potentially useful for mapping localized lateral changes in P-to-S conversion points.

To utilize the azimuthal dependencies in P-RFs that reflect the lateral changes in interface depths, we adopt a binned-stack approach with 10-degree ranges and intervals for both epicentral distance and back-azimuth to estimate the azimuth-dependent P-RFs. To maintain a high-quality dataset in this stacking process, we employ the cross-correlation-based selection method (Tkalčić et al., 2011), as in Taira and Yoshizawa (2020). This method selects P-RF traces for stacking based on normalized cross-correlation coefficients (NCC) between all P-RF pairs. In this study, we grouped P-RF traces with NCC > 0.8 for the 0.03–0.2 Hz range and NCC >0.7 for the 0.03–0.5 Hz range, discarding groups with fewer than 10 traces.

Figure 2 shows examples of azimuth-dependent P-RF dataset for CTAO, located in northwestern Australia. Figure 2 (a) presents a map of events used to compute the RFs visualized in Figures 2 (b) and (c). While both P-RFs reflect the seismic structure beneath CTAO, the expected conversion points differ laterally by 100–150 km at 200 km depths. In Figures 2 (b) and (c), distinct differences in the shapes of back-azimuth-ordered and stacked RFs are visible (e.g., at 5, 8, and 20 s). Around 5 s, the stacked P-RF from western events (green line in Figure 2 (c)) clearly exhibits a positive signal, which is unclear in the stacked P-RF from eastern events (green line in Figure 2 (b)). Around 8 s in the eastern P-RFs (Figure 2 (b)) and 20 s in the western P-RFs (Figure 2 (c)), strong negative phases are evident. Besides, these differences in azimuth-dependent P-RFs seem to be coherent within each back-azimuth range (left panels in Figures 2 (b, c)), implying structural variations beneath the station along the ray-paths.

Figure 3 (a) displays a compilation of stacked P-RFs at CTAO as a function of back-azimuth, along with a schematic illustration of the plausible origin of these azimuthal dependencies (Figure 3 (b)). The event distribution used for the azimuth-dependent RFs at CTAO is shown in Figure S3 (a). Figure S4 shows the frequency dependence of azimuth-dependent P-RFs at CTAO, covering four frequency ranges (i.e., 0.03–0.125 Hz; 0.03–0.2 Hz; 0.03–0.5 Hz; 0.04-1.0 Hz). In Figure 3 (a), as described, P-to-S conversions appear as isolated phases at around 5 s in the western and northern directions, whereas in the east, these conversions become less distinct due to overlap with the direct P-wave. In higher frequency ranges (Figure S4 (c, d)), the positive phases at 5 s are more prominent than in lower frequency P-RFs (Figure 3 (a)). Additionally, at higher frequencies, remarkable differences also emerge before the Moho conversions, potentially indicating lateral variations in crustal structure, although this is beyond our current scope. In the later phases (after 5 s), significant negative phases around 20 s appear in the west and north directions, but these negative phases are absent in the eastern P-RFs. These trends remain consistent in the higher frequency P-RFs (Figure S4) and appear robust, although the high-frequency energy becomes somewhat less clear than at lower frequencies due to contamination from multiple reflections from the Moho, shallower interfaces, and other scattered phases.

The significant negative phases at 20 s likely originate from a rapid velocity reduction in the upper mantle. Around CTAO, previous tomographic models have suggested that the upper mantle structure undergoes rapid lateral changes, possibly reflecting the transition between the eastern Phanerozoic and western cratonic regions (e.g., Fishwick et al., 2008; Yoshizawa, 2014; de Laat et al., 2023). Figure 3 (b) provides a schematic illustration of Ps conversion points with and without such structural changes. Conventional RF studies in continental regions have implicitly assumed a 1-D stratified layered model beneath the station (left panel in Figure 3 (b)). However, in the scenario depicted in the right panel of Figure 3 (b), the conversion points from P to S vary with the incoming direction of teleseismic P-waves, which serve as the parent phase for the converted S-waves. The azimuth-dependent P-RFs observed at CTAO likely result from lateral localized variations in the upper mantle interface.

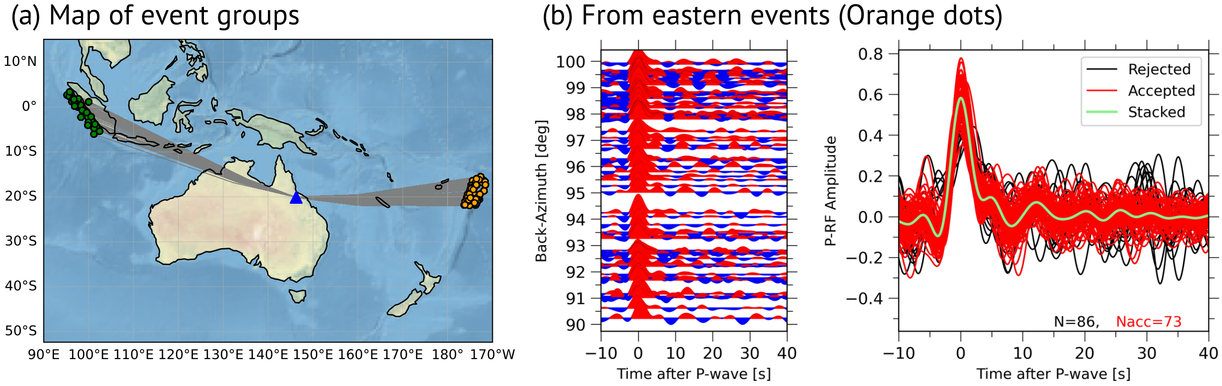
(a) Map of event groups

(b) From eastern events (Orange dots)

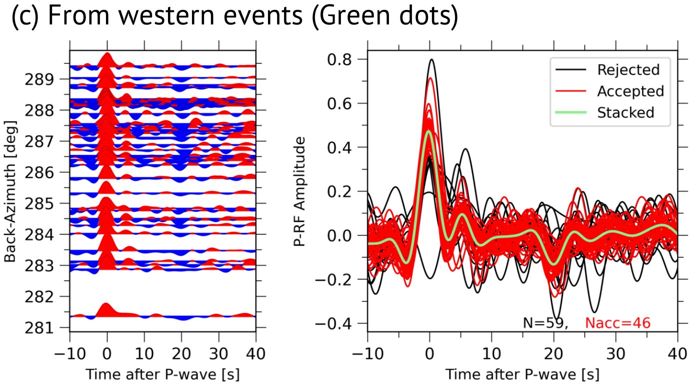
(c) From western events (Green dots)

Figure 2: Example of the binned-stacking process for P-RFs at CTAO. (a) Map of seismic events for two groups, with orange and green dots representing eastern and western events, respectively. Gray lines indicate ray paths from each event location to the station. (b) P-RF stacking process for the eastern event group (orange dots in (a)) with a back-azimuth range between 90° and 100°. The left panel shows individual P-RF traces that meet all selection criteria outlined in the main text, with positive and negative phases filled in red and blue. The right panel shows the stacking process, where green, red, and black lines represent stacked, accepted, and rejected traces based on cross-correlation selection. N and N_{acc} denote the total number of traces and the number of accepted traces, respectively. (c) Same as (b) but for the western event group (green dots in (a)).

Figure 4 shows azimuth-dependent P-RF datasets (0.03–0.2 Hz) at four stations, excluding CTAO: (a) G.CAN (b) IU.MBWA, (c) IU.NWAO, and (d) II.WRAB. Figure 4 (e) shows the distribution of all events used in this study, while Figure S3 displays the event distributions used for the RF analyses at each station. Figure S5 presents the shorter-period datasets (0.03–0.5 Hz) for these stations. Except for MBWA (Figure 4 (b)), clear positive conversion phases are observed at 5–6 s in Figures 4 (a), (c), and (d), suggesting the thick crust or the deep Moho (Kennett et al., 2023). On the contrary, the lack of positive phases at 5 s in MBWA may indicate the thinner crust, around 30 km in thickness (e.g., Taira and Yoshizawa, 2020; Kennett et al., 2023), which is also shown in Figure S5 (b). As shown in MBWA (Figure 4 (b)), long-period P-RFs may not adequately constrain the Moho depth and crustal structure in regions with thinner crust. Thus, we used higher-frequency data (0.03–0.5 Hz) from 10 s after the main P-phase in the inversion process described in the next section. For four stations (Figure 4 (a-d)), the later phases after 5–6 s exhibit the azimuthal variations in both amplitudes and arrival (or lag) times, although this tendency is weaker than that observed at CTAO (Figure 3 (a)), implying that lateral variations in seismic structure beneath these stations may be milder.

3. Trans-dimensional Bayesian inversion

We apply hierarchical trans-dimensional Bayesian inference (Bodin et al., 2012) to invert azimuth-dependent P-RFs and multimode SWDs (phase speeds of Rayleigh and Love waves). This probabilistic approach allows for flexible sampling of model parameters and requests fewer a priori constraints than traditional linearized inversion methods. The

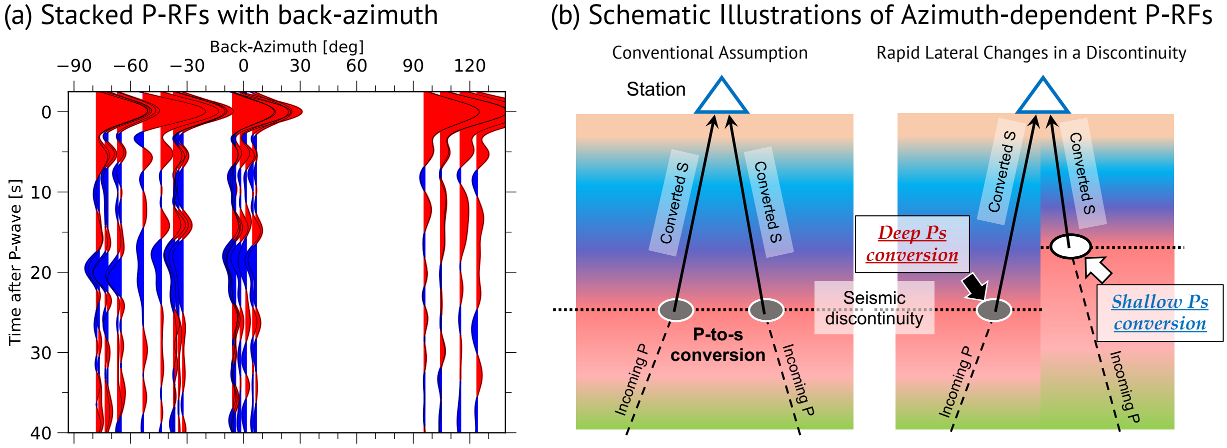

Figure 3: Azimuth-dependent P-RF dataset for CTAO and schematic illustrations of azimuthal dependence in P-RFs. (a) Compilation of stacked P-RF traces at CTAO with respect to back-azimuth, measured clockwise from the north. The color scheme for filled phases is the same as the right panels in Figures 2 (b and c). (b) Schematic illustrations of potential origins of azimuthal dependence in P-RFs. The left panel shows the P-to-S conversion assuming a 1-D stratified model, where conversion locations are independent of the incoming P-wave directions. In contrast, the right panel illustrates a scenario with rapid lateral structural changes around the seismic station, where conversion points vary with the event's azimuth.

trans-dimensional algorithm treats both the number of parameters (e.g., the number of layers) and data uncertainties as unknowns, allowing for exploration across the entire model parameter space. We consider the Bayesian theorem extended into a hierarchical trans-dimensional formulation as follows,

$$p(\mathbf{m}(k), k, \boldsymbol{\sigma} \| \mathbf{d}) \propto p(\mathbf{d} \| \mathbf{m}(k), k, \boldsymbol{\sigma}) p(\mathbf{m}(k)) p(k) p(\boldsymbol{\sigma}), \tag{1}$$

where $p(A\|B)$ is the conditional probability density function (p.d.f.) of the occurrence of A given B. $p(m(k), k, \boldsymbol{\sigma}\|d)$, $p(d\|m(k), k, \boldsymbol{\sigma})$, $p(m(k))$, $p(k)$, and $p(\boldsymbol{\sigma})$ represent the posterior, likelihood, model prior, hyperpriors for the number of model parameters and the data noise, respectively. To estimate the posterior probability, we employ the reversible-jump Markov chain Monte Carlo (RJMCMC) method (Green, 1995), which efficiently samples model parameters to fit the observed data.

3.1. Model parameterization

In this study, we assume a one-dimensional stratified structure beneath each station. The stratified model parameters follow Taira and Yoshizawa (2020), comprising interface depths z and perturbations in SV and SH wave velocities from the reference model, δV_{SV} and δV_{SH}. Using the hierarchical trans-dimensional scheme, we also include hyperparameters to be recovered; i.e., data noises $\boldsymbol{\sigma}$ for 12 data sets, including P-RFs for two frequency ranges and the multimode dispersion curves (0th – 4th modes) of Rayleigh and Love waves, and the number of layers k. Thus, the model parameter vector $\mathbf{m}$ is defined as $[\boldsymbol{\sigma}, k, \mathbf{z}, \delta\mathbf{V}_{\mathbf{SV}}, \delta\mathbf{V}_{\mathbf{SH}}]$.

The spherical radially anisotropic S-wave model is perturbed to the 400 km depth, combined with the PREM (Dziewonski and Anderson, 1981) below 400 km. Other elastic parameters are scaled based on the shear-velocity structure and replaced by the 1-D reference model. For P-waves, we maintain the fixed ratio between V_P and V_S to the AK135 model (Kennett et al., 1995) and calculate V_P from V_S. The density structure ρ is scaled with compressional wave speeds through the empirical relationship $\rho = 2.35 + 0.036(V_P - 3)^2$ (e.g., Tkalčić et al., 2006; Bodin et al., 2012, 2014; Taira and Yoshizawa, 2020). The radial anisotropy parameter η and anelastic attenuation values of Q_κ and Q_μ are fixed to a modified PREM where the 220 km discontinuity is smoothed.

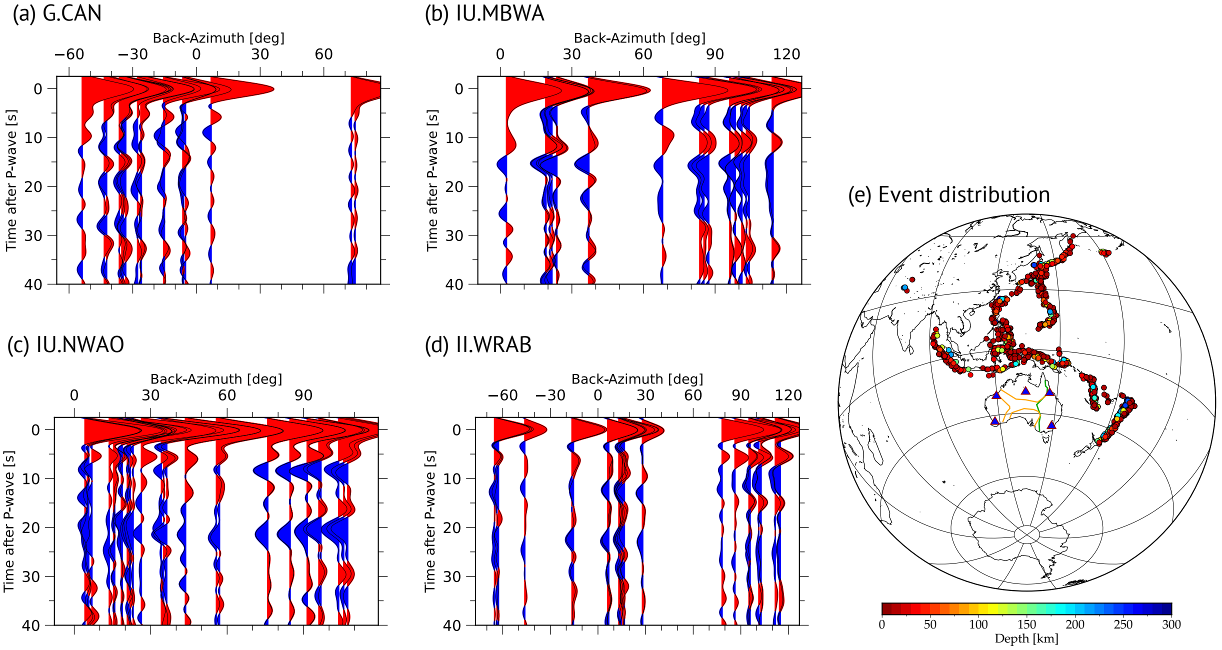

Figure 4: (a–d) Azimuth-dependent P-RF datasets (0.03–0.2 Hz) of the four stations used in this study: (a) G.CAN, (b) IU.MBWA, (c) IU.NWAO, and (d) II.WRAB. Figure notations are the same as Figure 3 (a). (e) Map of all events used in this study, with blue triangles indicating station locations and colored circles representing individual seismic events. Yellow and green lines delineate the major cratonic boundaries and the Tasman Line.

3.2. The prior

Prior probabilities for model parameters are defined using uniform or normal distributions. For the number of parameters k and data uncertainties $\boldsymbol{\sigma}$, we assume uniform distributions over the ranges [5, 61] and [0.01, 0.2], respectively. The prior for the depth is uniformly distributed from 0 to 400 km.

For S-wave perturbations, we use a zero-mean Gaussian prior with a standard deviation of $\sigma = 0.3$ km/s, following Akuhara et al. (2021) and Ai et al. (2023). Local reference models for each station are derived from the three-dimensional radially anisotropic S-wave speed model by Yoshizawa (2014), which has been optimized for multimode SWDs through linearized inversions, providing good resolution in the deep upper mantle. The crustal model, however, is approximated using the 3SMAC model (Nataf and Ricard, 1996) since phase velocities from seismic surface waves at periods longer than 30 s have limited sensitivity to shallow structures. To represent the Australian crustal structure accurately, we replace the crustal SV velocity model of Yoshizawa (2014) with the AuSREM crustal S-wave speed model and local Moho depth (Kennett et al., 2011; Salmon et al., 2013; Kennett et al., 2023). Radial anisotropy is fixed to the Yoshizawa (2014) model. As a result, our local reference model reflects both the crustal and upper mantle structure of Australia. Figure S6 displays the reference structural model used for each station.

3.3. Likelihood function

The likelihood functions measure the consistency between synthetic and observed data. Since we incorporate both surface-wave dispersion curves and P-RFs, our likelihood term is defined by the joint probability:

$$p(\mathbf{d}\|\mathbf{m}(k),\sigma) = p(\mathbf{d}_{\mathbf{SWD}}\|\mathbf{m}(k),\boldsymbol{\sigma}_{\mathbf{SWD}})\; p(\mathbf{d}_{\mathbf{PRF}}\|\mathbf{m}(k),\boldsymbol{\sigma}_{\mathbf{PRF}}), \tag{2}$$

where the first and second terms in the right-hand of (eq. 2) correspond to the likelihood probability density functions for SWD and P-RF, respectively. These are formulated based on the Gaussian distributions following Taira and

Yoshizawa (2020):

$$p(\mathbf{d_{SWD}}\|\mathbf{m}(k),\sigma_{\mathbf{SWD}}) = \prod_{i=0}^{4}\frac{1}{\sigma_i^{\mathrm{R}}\sqrt{(2\pi)^{N_{\mathrm{R}_i}}}}\exp\left(-\frac{\|\mathbf{d}_i^{\mathrm{R}}-\mathbf{g}_i^{\mathrm{R}}(\mathbf{m}(k))\|^2}{2\sigma_i^{\mathrm{R},2}}\right)$$
$$\times\prod_{i=0}^{4}\frac{1}{\sigma_i^{\mathrm{L}}\sqrt{(2\pi)^{N_{\mathrm{L}_i}}}}\exp\left(-\frac{\|\mathbf{d}_i^{\mathrm{L}}-\mathbf{g}_i^{\mathrm{L}}(\mathbf{m}(k))\|^2}{2\sigma_i^{\mathrm{L},2}}\right), \tag{3}$$

and

$$p(\mathbf{d_{PRF}}\|\mathbf{m}(k),\sigma_{\mathbf{PRF}}) = \prod_{i=1}^{2}\frac{1}{\sigma_i^{\mathrm{PRF}}\sqrt{(2\pi)^{N_{\mathrm{PRF}_i}}}}\exp\left(-\frac{\|\mathbf{d}_i^{\mathrm{PRF}}-\mathbf{g}_i^{\mathrm{PRF}}(\mathbf{m}(k))\|^2}{2\sigma_i^{\mathrm{PRF},2}}\right), \tag{4}$$

where i denotes the mode number of Rayleigh and Love waves in (3), as well as the two frequency bands for the P-RFs in (4). $\mathbf{d}^R$, $\mathbf{d}^L$, and $\mathbf{d}^{PRF}$ represent the observed data for Rayleigh and Love wave dispersion curves and P-RFs, respectively, and $\mathbf{g}^R$, $\mathbf{g}^L$, and $\mathbf{g}^{PRF}$ denote the forward-modeled data for each dataset. For synthetic data calculations, we use the normal mode theory (DISPER80; Takeuchi and Saito, 1972; Saito, 1988) for SWD computations and the Thomson-Haskell method (Thomson, 1950; Haskell, 1962) for P-RF modeling, which is widely used in Monte-Carlo inversion studies (e.g., Bodin et al., 2012, 2016; Calò et al., 2016; Taira and Yoshizawa, 2020). Since these approaches are based on a 1-D stratified flat Earth model, we apply an Earth-flattening correction to account for the spherical Earth model.

In the RF modeling, we adopted the conventional water-level method for spectral division, using the same flat-level damping factor as described in Section 2. To reduce the computational cost associated with the time-consuming MCMC-based Bayesian inversion, we did not apply our modified multi-taper spectral estimation (Text S1) to the synthetic RFs. Instead, spectral estimation for the synthetic RFs was performed using a single-taper (cosine-taper) FFT, followed by spectral division with the same flat-level damping criterion used for the observed RFs. This approach ensures consistency in the spectral division between the observed and synthetic RFs. The potential influence of differences in the spectral estimation step is evaluated and validated in Text S2 and Figures S7–S9 of the Supplementary Material, confirming that these differences do not significantly affect the final inversion results.

To investigate the lateral variations of discontinuity depths, we performed inversions using local SWDs from the surface-wave tomography model as well as P-RFs for each azimuth-distance bin. Note that the local multimode SWDs were fixed for each station (Figure S2) because they reflect the local seismic structure around a seismic station as seen by long-wavelength surface waves.

3.4. Reversible-jump sampling with Parallel Tempering

To estimate ensemble solutions, we use the reversible-jump Markov chain Monte Carlo (RJMCMC) scheme (Green, 1995). RJMCMC aims to infer the posterior density of model parameters by iteratively exploring model parameter spaces of varying dimensions. In each iteration, a new model parameter vector is proposed by randomly selecting one of several perturbation patterns: (1) create a new layer, (2) remove a layer, (3) perturb a data error, (4) adjust a transition depth, (5) perturb the SV wave speed in a layer, or (6) perturb the SH wave speed in a layer. We then compute the synthetic data and likelihood function based on the proposed model. The model acceptance is determined using the Metropolis-Hastings (MH) algorithm (Metropolis et al., 1953; Hastings, 1970). To enhance convergence speed and improve acceptance rates, we apply the Parallel Tempering (PT) method to the MH algorithm (Sambridge, 2014), as implemented in Taira and Yoshizawa (2020) and Akuhara et al. (2021). PT enables broader exploration of the model parameter space by running multiple Markov chains in parallel, each with a different temperature. Consequently, our MH acceptance criterion, based on the likelihood probability, is expressed as:

$$\alpha_{MH} = \min\left\{1, \left[\frac{p(\mathbf{d}\|\mathbf{m}_j,k_j,\boldsymbol{\sigma}_j)}{p(\mathbf{d}\|\mathbf{m}_i,k_i,\boldsymbol{\sigma}_i)}\right]^{1/T_j}\times\left[\frac{p(\mathbf{d}\|\mathbf{m}_i,k_i,\boldsymbol{\sigma}_i)}{p(\mathbf{d}\|\mathbf{m}_j,k_j,\boldsymbol{\sigma}_j)}\right]^{1/T_i}\right\}, \tag{5}$$

where α_{MH} is the acceptance probability in the PT framework, subscripts i and j denote the i-th and j-th MCMC chains, and T_n is the temperature of the n-th chain. In PT, each chain runs in parallel at a different temperature. In this study, we run 40 chains in parallel, 10 of which are set as unit temperature, while the remaining 30 chains have higher temperatures following $T_i = 200^{i/30}$, resulting in a maximum temperature of 200 °C.

For RJMCMC sampling, we set the maximum iteration number of 150,000, discarding the initial 50,000 models as the burn-in period. To avoid autocorrelated samples, we store the models at intervals of 100 iterations, resulting in posterior distributions constructed from 10,000 models.

4. Results of inversions for Australian stations

The trans-dimensional Bayesian inversion estimates the probability density functions of model parameters. From these probabilistic models, we identify seismic discontinuities (i.e., Moho, LAB, MLDs, and X-Ds) based on S-wave velocity changes through a combination of automated and visual inspections. Hereafter, we focus on the isotropic S-wave speed derived by the voigt average, $V_{S_{iso}} = \sqrt{\frac{2V_{SV}^2+V_{SH}^2}{3}}$, and the radial anisotropy, $\xi = (\frac{V_{SH}}{V_{SV}})^2$.

Using our posterior distributions, the Moho can be identified as the depth of the maximum positive V_{iso} jump, mostly consistent with the AusMoho depth (Kennett et al., 2023) constructed by compiling multiple geophysical datasets (e.g., reflection profiles and refraction explorations). S-wave speeds in the asthenosphere are generally slower than the lithosphere, and the LAB is often characterized by the significant S-wave speed reduction in the upper mantle (e.g., Kennett et al., 2013). Thus, we first imposed an isotropic S-wave speed of less than 4.7 km/s as an LAB criterion, then determined the LAB as a V_{iso} or V_{SV} drop of over 0.04 km/s around the Lithosphere-Asthenosphere Transition (LAT) identified by Yoshizawa (2014) from vertical gradients in shear wave speed profiles. However, at WRAB in the southern North Australian Craton (NAC), the high isotropic S-wave speed extends to 200–300 km depth, and no significant velocity reduction is observed within the LAT range. In such cases, we determined the depth of the lithospheric base by identifying a positive jump in radial anisotropy, ξ, following Plomerová et al. (2002).

With the mantle lithosphere thickness defined, we identified MLDs within the mantle lithosphere and X-Ds underlying the LAB or lithospheric base. MLDs are marked by a V_{iso} or V_{SV} change of at least 0.02 km/s above the LAT upper bound or selected LAB depths and are detected primarily at stations in cratonic areas (MBWA, NWAO, and WRAB). For X-Ds, we identified S-wave speed jumps of over 0.04 km/s beneath the selected LAB. Both MLDs and X-Ds may occur at multiple depths. To examine the relationship between MLDs/X-Ds and the radial anisotropy without bias, we did not adopt any criteria related to radial anisotropy when identifying MLDs and X-Ds.

This section discusses our results separately for the Phanerozoic and cratonic provinces of Australia. For the Phanerozoic province, we present inversion results for CTAO and CAN (Figures 5 and 6). For cratonic regions, Figure 7 shows joint inversion results at two stations, MBWA and NWAO, in the WAC, and Figure 8 presents the results at WRAB in the NAC. Employed event distributions are also displayed in Figures 5, 6, 7, and 8. Previously estimated discontinuity depths from earlier studies (Yoshizawa, 2014; Birkey et al., 2021; Kennett et al., 2023) are superimposed on the resultant 1-D profiles, including AusMoho depth, the first and second negative peaks in S-RF profiles from Birkey et al. (2021), and LAT upper and lower bounds from Yoshizawa (2014), as indicated in each figure and caption.

4.1. Phanerozoic eastern Australia

4.1.1. CTAO station

Selected inversion results at the CTAO station for the eastern, western, and northern event groups are shown in Figure 5. Posterior distributions for hyperparameters (i.e., the number of layers and data noises) and data misfit distributions are summarized in Figures S10-S12. In the inversion results at CTAO, distinct azimuthal dependencies are observed in both isotropic S-wave and radial anisotropy profiles (Figure 5 (b–d)). The data misfits are sufficiently low, with each P-RF well reproduced (Figures S10, S11, and S12), indicating that the velocity structures are reliably resolved. Identified upper mantle discontinuities vary with the incident directions of teleseismic P-waves corresponding to each event group.

In all inversion results (Figure 5 (b–d)), we observe shear wave speed jumps at around 40 km, corresponding to the Moho, consistent with the AusMoho model (Kennett et al., 2023)) and Taira and Yoshizawa (2020). Some variations in crustal structures are present in the results for different event directions but are not discussed here, as our focus is on the upper mantle discontinuities. Note that our long-period SWD dataset has limited sensitivity to constrain the absolute shear velocity in the crust.

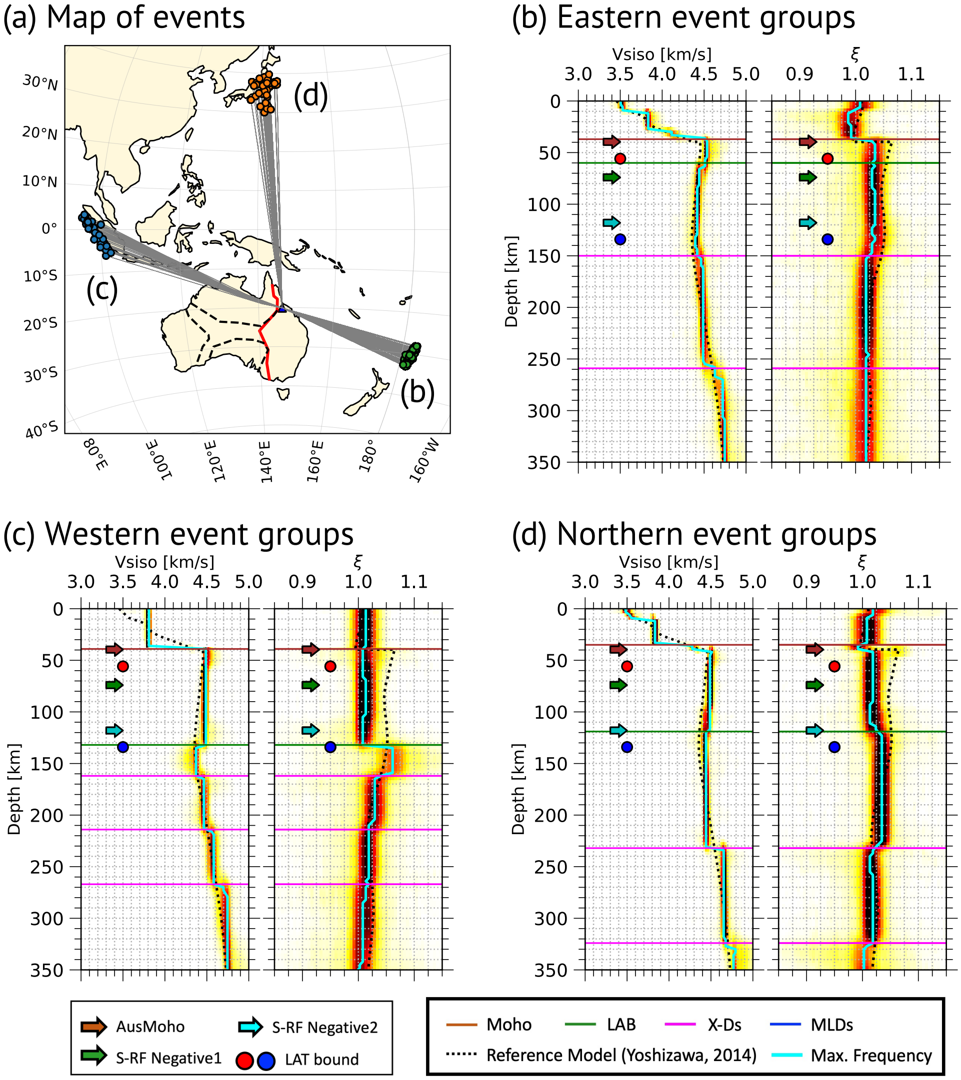

Figure 5: Examples of joint inversion results for CTAO. (a) Event distribution, with colored dots representing seismic events grouped by direction and a blue triangle indicating the target station. Black dotted and red lines are the major cratonic boundaries and the Tasman Line, respectively. (b) Posterior distributions of isotropic S-wave speed V_{iso} and radial anisotropy ξ retrieved from the eastern event group, with cyan lines indicating the maximum frequency (i.e., mode) models, respectively. Black dotted lines show the reference model for the inversion. Colored horizontal lines are identified discontinuities (brown: Moho, blue: MLDs, green: LAB or Lithospheric base, magenta: X-Ds). Brown arrows indicate the AusMoho depth Kennett et al. (2023), while green and light blue arrows represent the depths of the first and second maximum negative peaks in S-RF profiles (Birkey et al., 2021). Red and blue dots exhibit the upper and lower depths of the Lithosphere-Asthenosphere Transition (LAT) derived from Yoshizawa (2014). All notations are shown at the bottom of the figure. (c, d) Same as (b), but for the western and northern event groups.

The LAB depths, marked by shear velocity reductions, vary by event group, suggesting lateral changes in lithospheric thickness. In the eastern results (Figure 5 (b)), an S-wave velocity drop appears at around 60 km within the LAT, which may be comparable to the S-RF's negative phase at 74 km (Birkey et al., 2021). Western and northern results show a deeper velocity drop at 120–130 km, above the lower bound of LAT (Figure 5 (c, d)), consistent with the second negative peak of S-RF at 118 km. Increasing radial anisotropy ξ below these interfaces (Figure 5 (b–d)) is consistent with the expected horizontal shear flow in the asthenosphere.

These findings suggest rapid lateral LAB depth variations around CTAO, from 60–70 km in the east to 120-130 km in the west and north, supporting a step-wise lithospheric model by Fishwick et al. (2008) and the azimuth-dependent variations seen in the P-RF profiles (Figure 3).

Below the LAB at CTAO, we identify multiple S-velocity jumps at around 170, 220, 270, and 330 km, consistent with Revenaugh and Jordan (1991), who proposed similar multiple discontinuities based on path-averaged ScS reverberations. They interpreted shallower interfaces around 170 and 220 km as the Lehmann discontinuity and the deeper interfaces as the X-Ds. Although we cannot decisively identify the Lehmann discontinuity, these multiple discontinuities, associated with positive S-velocity jumps, coincide with regions of weakened anisotropy, as noted in Taira and Yoshizawa (2020).

The estimated velocity structures shown in Figure 5 (b–d) reveal azimuth-dependent differences from the previously published multi-mode surface-wave tomographic model by Yoshizawa (2014), which represents the azimuthally averaged profile. In particular, the eastern result (Figure 5 (b)) appears to be consistent with the reference surface-wave model in both V_{iso} and ξ, whereas the western and northern results (Figure 5 (c, d)) exhibit a generally weaker anisotropic trend above the inferred LAB with faster V_{iso} at around 100 km depth. These results suggest that the eastern model may reflect the azimuthally averaged structural characteristics beneath CTAO.

4.1.2. CAN station

For the CAN station, obtained S-velocity profiles for different event groups are consistent (Figure 6), unlike the result for CTAO in Figure 5. Clear S-wave velocity jumps at 40 km depth indicate the Moho, which is slightly shallower than AusMoho. While the Australian Moho map (e.g., Kennett et al., 2023) suggests a locally thicker crust in southeastern Australia, its northern area indicates a thinner crust, which may be reflected in our results. The LAB is identified by a sharp velocity reduction at around 80 km depth within the LAT, similar to the S-RF negative peaks reported by Birkey et al. (2021). Like CTAO, the LAB is accompanied by a downward increase in radial anisotropy, suggesting the influence of horizontal mantle flow beneath it. Our data suggest an interface with a shear velocity drop at 65km depth (e.g., Figure S13), consistent with another negative S-RF phase at 50–60 km in Birkey et al. (2021). Below the LAB, we detect multiple discontinuities with positive velocity gradients and similar anisotropy characteristics to CTAO, showing decreased ξ. The detected depths are close to those at CTAO: 140-150 km, 220–260 km, and around 300 km.

4.2. Cratonic central and western Australia

4.2.1. MBWA and NWAO stations in western Australia

Figure 7 shows inversion results using multiple event groups for both the MBWA and NWAO stations located in the Archean cratons. At MBWA located near the northeastern margin of the Pilbara craton, facing the suture zone between WAC and NAC, azimuthal dependency is evident, likely due to the structural differences along the northern and eastern paths (Figure 7 (b, c)). In contrast, NWAO located in the southwestern area of the Yilgarn craton, where eastern and northern ray-paths propagate through the stable cratonic region, exhibits weaker azimuthal dependency (Figure 7 (e, f)). Our results from the northern event groups are generally consistent with the S-RF studies (Birkey et al., 2021).

At MBWA in Figure 7 (a-c), azimuth-independent Moho depths are observed around 30 km, consistent with AusMoho (Kennett et al., 2023). The LAB, characterized by a shear velocity drop (> 0.04 km/s), is estimated at 150 km in the north and 170–180 km in the east, with a weaker increase in radial anisotropy than in eastern Australia. Multiple MLDs are identified at the lithospheric depths, consistent with previous studies (Taira and Yoshizawa, 2020; Sun et al., 2018), showing decreasing radial anisotropy across the MLDs as suggested by Yoshizawa and Kennett (2015) and Kennett et al. (2017). The second and third MLDs (Figure 7 (b)) exhibit negative velocity changes, supporting the earlier S-RF study by Birkey et al. (2021). A single X-D is observed at around 270 km, accompanying the weakening of radial anisotropy.

At NWAO in Figure 7 (d-f), azimuth-independent Moho depths are identified at 40 km. MLDs are found at a depth of 60 km in the eastern path and 80 km in the northern path, similar to the results from S-RF (Birkey et al., 2021). LAB signatures are detected at 130 km depth in the northern path, which is consistent with the second negative peak in S-RF by Birkey et al. (2021), and at 100 km in the eastern path. The X-Ds under the LAB are seen in the range from 250 to 300 km, consistent with the depths identified by Taira and Yoshizawa (2020) at 270 km and the Lehmann discontinuity by Revenaugh and Jordan (1991) at around 255–280 km.

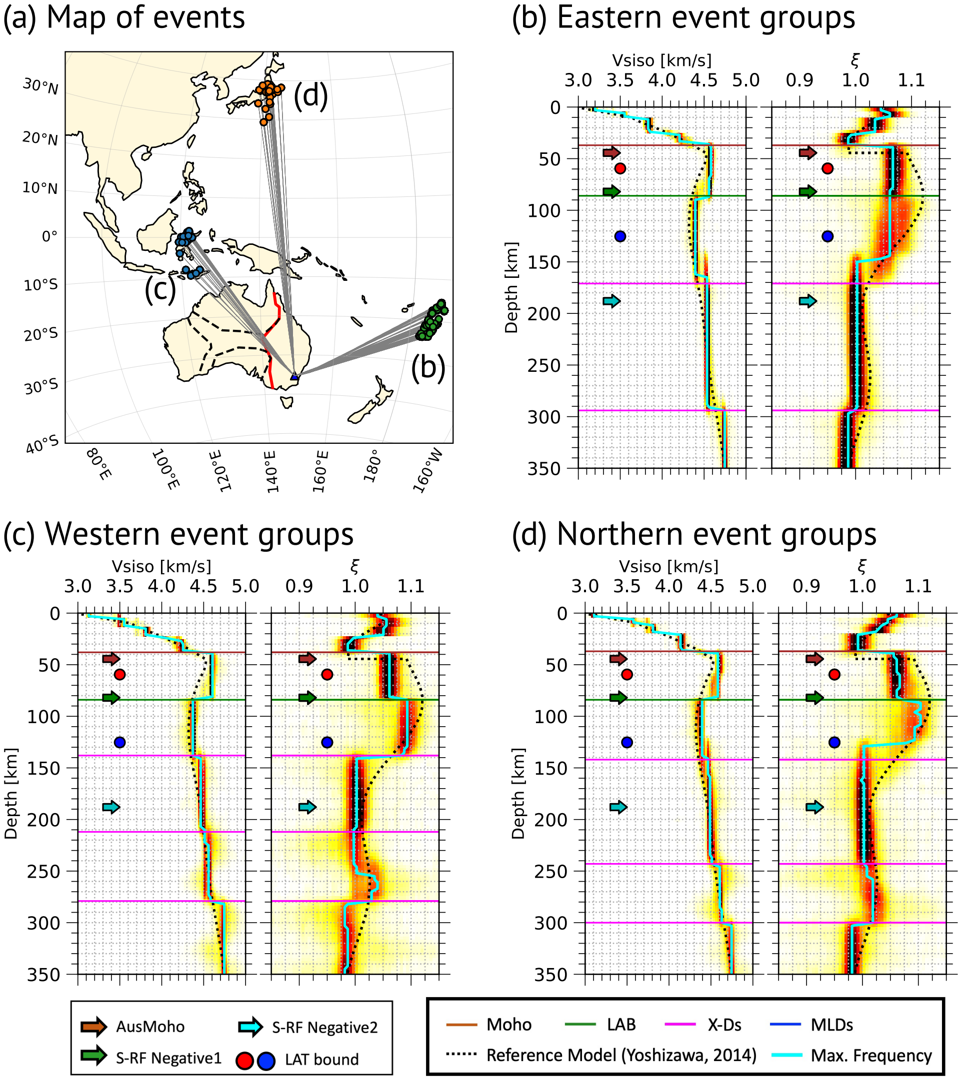

Figure 6: Same as 5, but for G.CAN.

4.2.2. *WRAB station in central Australia*

Figure 8 shows the inversion resultants at WRAB, located in the NAC, for three event groups. Despite being located in the stable craton, WRAB, three inversion results at WRAB display clear azimuthal dependence of radially anisotropic S-wave profiles (Figure 8 (b-d)). No significant S-wave speed drops are observed, and the signature of the asthenosphere or low-velocity zone is unclear beneath WRAB. A high-velocity structure (4.7–4.8 km/s) extends from just below the Moho (around 50 km) to the deep upper mantle, with a clear increase in radial anisotropy around the LAT.

For WRAB, the lithosphere base is defined by increased radial anisotropy, consistent with previous tomographic studies that indicate a thick high-speed region in the southern NAC (e.g., Yoshizawa, 2014; Magrini et al., 2023; de Laat et al., 2023). Despite the absence of a clear low-velocity zone in the AusREM model (Kennett et al., 2013), anomalous radial anisotropy with $V_{SH} > V_{SV}$ (Yoshizawa, 2014; Yoshizawa and Kennett, 2015) and the alignment of azimuthal anisotropy with plate motion direction (e.g., Simons et al., 2002; Fishwick et al., 2008; de Laat et al., 2023) suggest that the horizontal shear flow in the ductile asthenosphere drives the fast motion of the Australian plate. Thus, defining the lithosphere base via radial anisotropy can be a reasonable criterion.

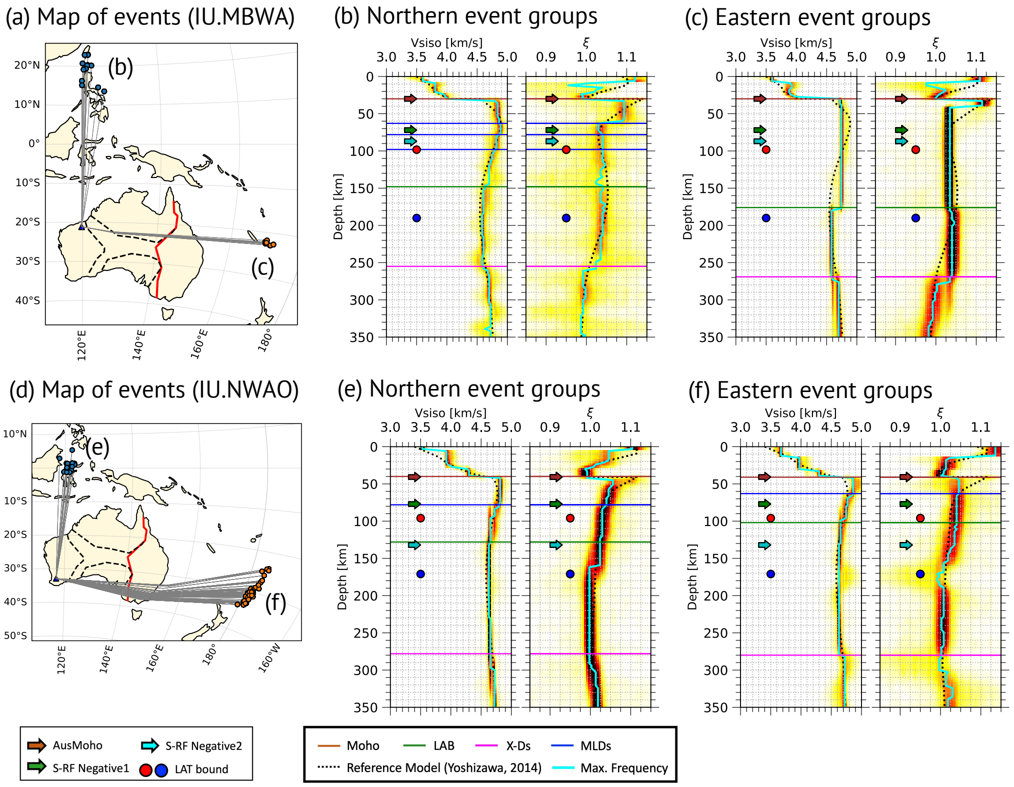

Figure 7: Same as Figure 5, but for IU.MBWA and IU.NWAO.

The estimated lithosphere base from the increased radial anisotropy for WRAB varies with the incoming P-wave directions: the western path indicates a thicker lithosphere of about 180 km, while the northern and eastern paths show a thinner lithosphere of about 120–130 km. X-Ds are detected at around 300 km, at which radial anisotropy is weakened and approaches isotropy (SH ≈ SV). In the lithospheric depth, we can identify minor S-wave velocity changes at 70-80 km depth in the northern and eastern paths, equivalent to MLD depths inferred from S-RFs (Birkey et al., 2021). However, our models show a positive velocity jump with decreasing anisotropy, contrasting with earlier MLD observations from S-RFs (Ford et al., 2010; Birkey et al., 2021).

5. Localized conversion point maps

After gathering Ps conversion depths for each discontinuity in the 1-D profiles, we created conversion point (CP) maps to visualize lateral variations of Ps-conversion depths around each station, representing the spatial distribution of seismic discontinuity. This approach is similar to Ford et al. (2010) with S-RFs, in which S-to-P conversion points tend to be distant from the station (≈ 250–350 km at 200 km depth). Our P-RF datasets provide the P-to-S conversion points within 100–150 km around the station, enabling more localized mapping of each discontinuity.

To estimate CP maps, at first, we constructed a local reference 1-D shear velocity model for each station from the average of the mode (maximum frequency) models for azimuth-dependent 1-D S-wave profiles (e.g., green lines in Figures 5, 6, 7 and 8). The P-wave structure is derived from the scaling of the S-wave based on AK135 (Kennett et al., 1995) as in the inversion. Then, the local 1-D reference model is used to compute ray paths to estimate the lateral locations of the Ps conversion points for the azimuth-dependent boundary depths explained in the previous section. To quantify the uncertainties of our depth estimations, we employed interquartile ranges (IQR) for each discontinuity depth from the ensemble solutions, as the resultant probabilistic densities do not always follow the Gaussian distribution.

Resultant CP maps and their depth uncertainties are shown in Figures 9 and 10 for two Phanerozoic stations and Figures 11 and 12 for three cratonic stations, including Moho, MLDs, LAB, and X-Ds. In this section, we investigate

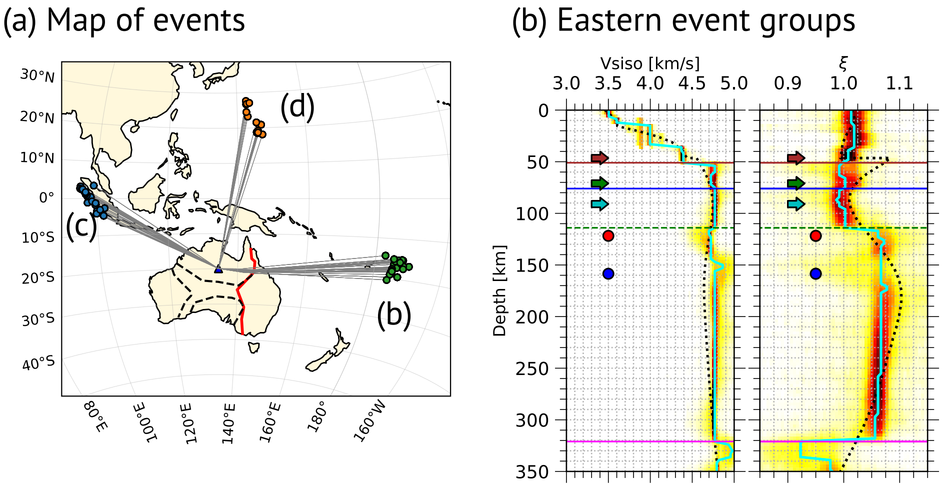
(a) Map of events

(b) Eastern event groups

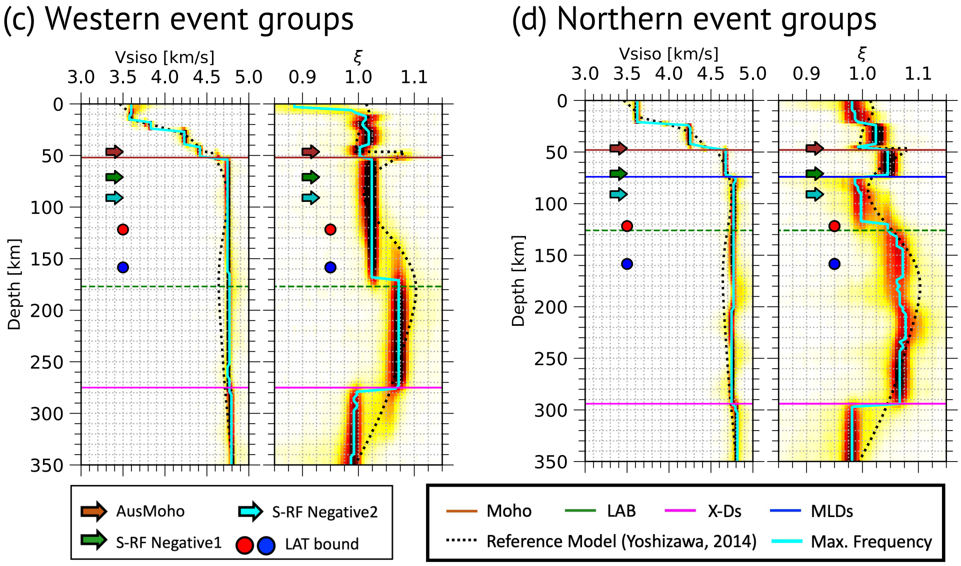
(c) Western event groups

(d) Northern event groups

Figure 8: Same as Figure 5, but for II.WRAB. The horizontal green dashed lines represent the estimated base of the lithosphere (relevant to LAB but identified based on radial anisotropy).

the spatial distribution of seismic discontinuities around each station based on these CP maps. In addition, Figure S14 displays the piercing point maps for Ps phases, calculated using the average slowness and back-azimuth of the binned-stacked P-RFs, which helps to interpret the expected CP distributions.

5.1. Phanerozoic eastern Australia

Figures 9 and 10 show CP maps and uncertainties (derived from IQR) for the Moho, LAB, and X-Ds around CTAO and CAN stations. Due to the limitations of event distributions, southern areas for both stations are unsampled, so we focus on the northwestern, northern, and eastern CPs. The IQR for the Moho are small (≈ 3 km), while those for deeper interfaces are relatively large (≈ 10 km).

5.1.1. Moho, LAB, and X-Ds in eastern Australia

For the Moho, CP depths (left panels in Figure 9) exhibit almost no significant azimuthal dependence at both stations, suggesting a nearly consistent crustal thickness. Around CAN, our results reflect somewhat shallower northern

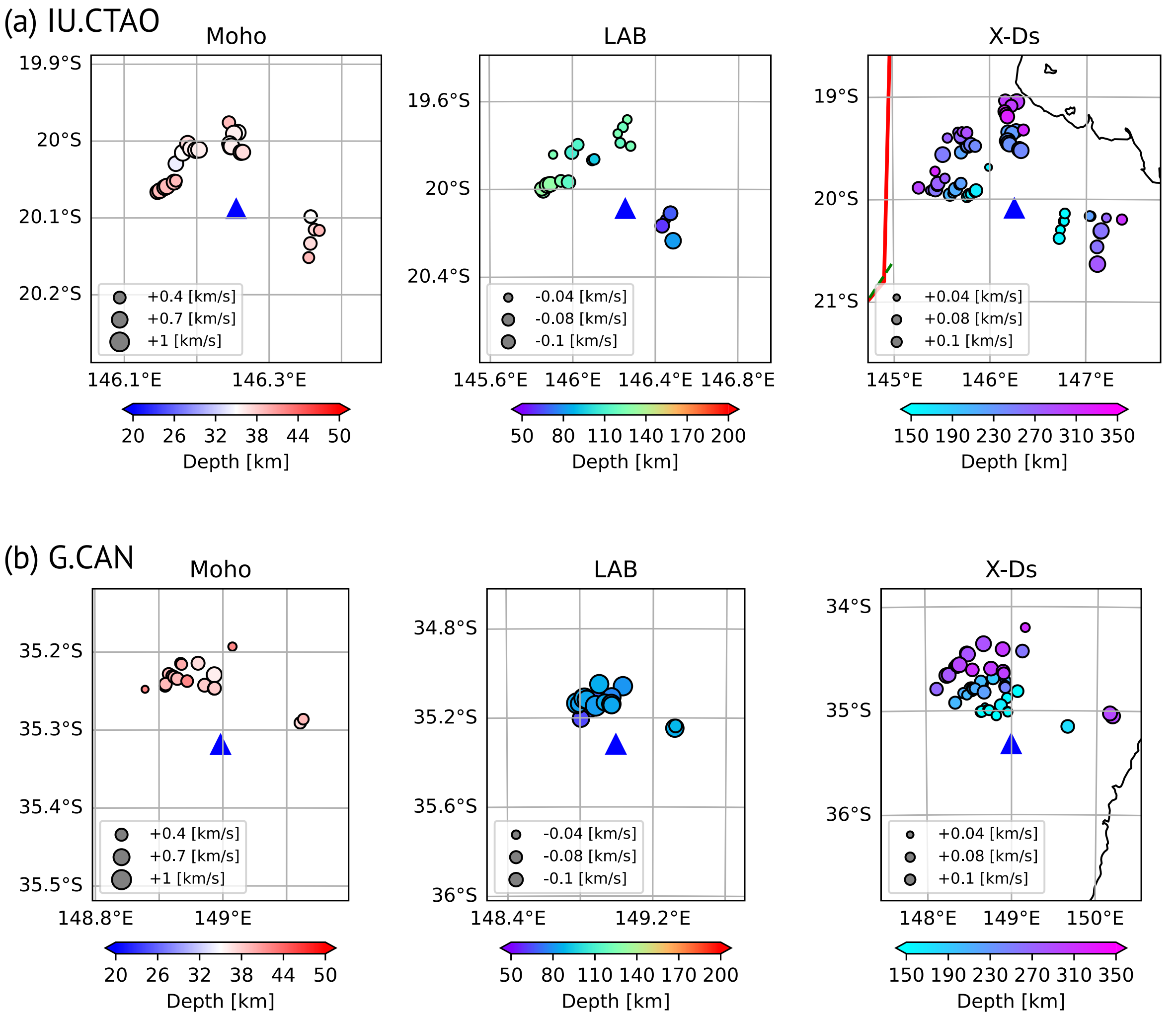

Figure 9: Conversion points (CPs) maps for Moho, LAB, and X-Ds at two stations in eastern Australia: (a) IU.CTAO and (b) G.CAN. For each station, the CP maps for Moho, LAB, and X-Ds are shown from left to right. A red line in the rightmost panel of (a) indicates the Tasman line. Blue triangles on all maps represent the station locations. Circles indicate the inferred Ps conversion locations, with color and size representing the depth and magnitude of the shear wave velocity across the interface.

Moho depths, aligning with Kennett et al. (2023). Similarly, CTAO shows a nearly constant Moho depth at around 40 km.

In contrast, the CP maps of the LAB (middle panels in Figure 9) reveal distinct images for each station, consistent with inversion results (Figures 5 and 6). At CTAO, LAB depths increase from east to west, with the depth ranging from 70 km to 120–130 km, supporting a stepwise lithospheric thickening at the eastern continental margin (Fishwick et al., 2008) and the rapid deepening of the LAT upper bound to the northwest of CTAO (Yoshizawa, 2014). At CAN, however, the LAB depth remains consistent at 65–80 km, suggesting stable lithospheric thickness to the north, as seen in previous models (Fishwick et al., 2008). Also, S-wave reductions are more pronounced at CAN, as observed in the tomography model by Yoshizawa (2014).

The CP maps of X-Ds (right panels in Figure 9) indicate multiple interfaces with positive shear wave speed jumps clustered around 170 km, 250 km, and 310 km. The shear wave speed changes across these interfaces are smaller than those across the LAB, likely undetectable by long-wavelength surface waves only. In the similar depth ranges, Taira and Yoshizawa (2020) identified two interfaces at 230–240 km and 300–310 km, and Revenaugh and Jordan (1991)

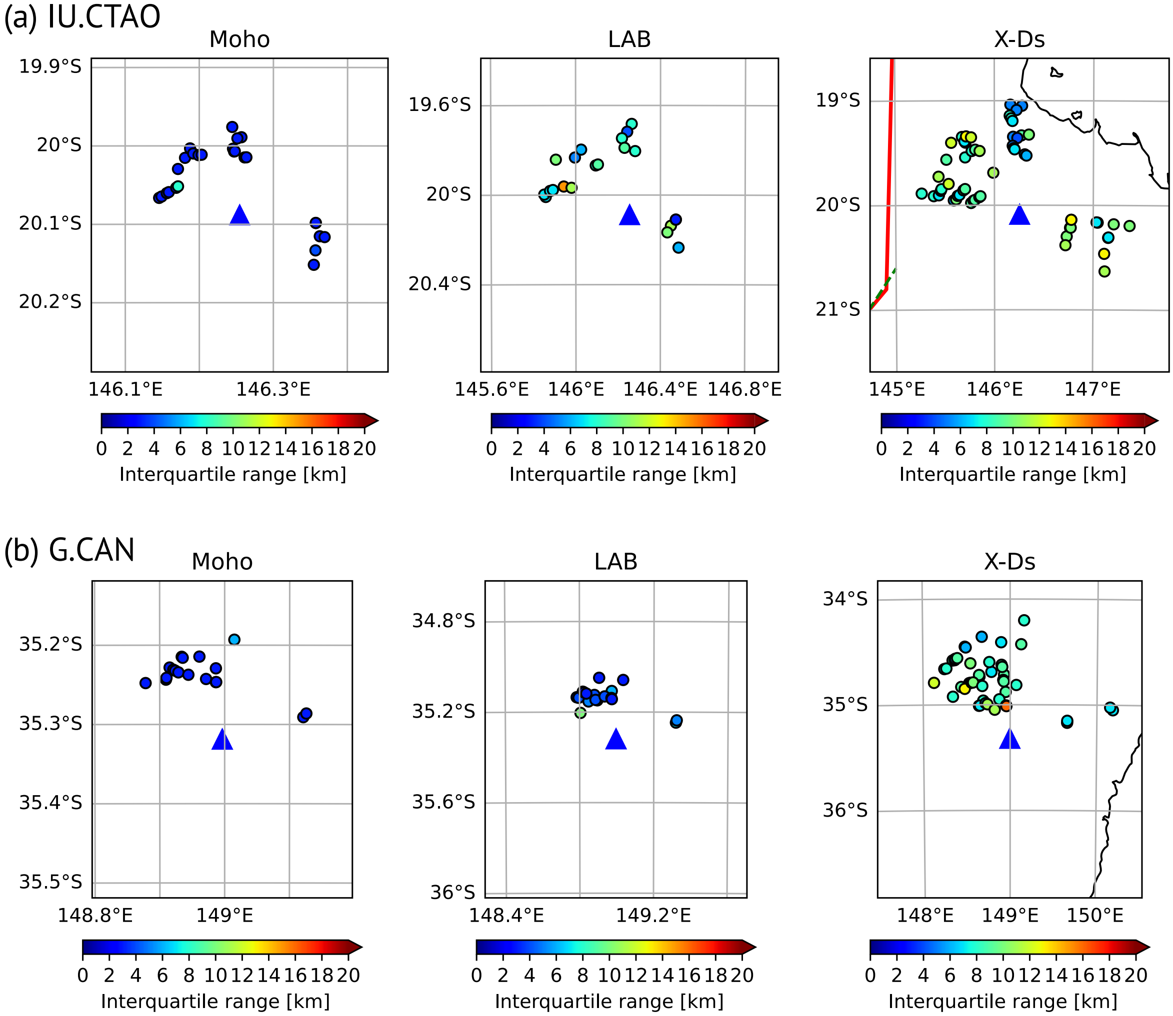

Figure 10: Depth uncertainties of conversion depths for Moho, LAB, and X-Ds: (a) IU.CTAO and (b) G.CAN. Circles are the location of conversion points, with colors indicating the interquartile ranges.

also detected two interfaces at 180–220 km (the Lehmann discontinuity) and around 330 km (X-D), although our CP maps for X-Ds suggest three or four distinct interfaces beneath the LAB.

5.2. Cratonic central and western Australia

Figure 11 displays CPs from the Moho, MLDs, LAB (or lithospheric base), and X-Ds at MBWA, NWAO, and WRAB stations, and Figure 12 shows the uncertainties of discontinuity depths based on IQR. Note that, unlike Figure 9 for stations in eastern Australia, where MLD is generally unclear, we add the MLD's CP map in Figure 11 in the mid-left panels, with circles and crosses indicating negative and positive S-wave speed changes, respectively. For WRAB, the mid-right panel represents the lithospheric thickness estimated from radial anisotropy as described in Section 4.2.2.

Except for the lithospheric base beneath WRAB, Figure 12 exhibits the IQRs for the upper mantle discontinuities (MLD, LAB, and X-Ds) are generally around 10–15 km, which are greater than those in the eastern Phanerozoic area (Figure 10). Larger uncertainties in the LAB depth possibly reflect the ambiguous transition from the lithosphere to the asthenosphere under the cratonic areas (e.g., Yoshizawa, 2014). Besides, the lithospheric base under WRAB shows larger IQRs than the other two cratonic stations, MBWA and NWAO (Figure 12). These results are expected from the somewhat ambiguous definition of the lithospheric base using radial anisotropy since the horizontally polarized S velocity (V_{SH}) cannot be constrained by the receiver functions.

(a) IU.MBWA

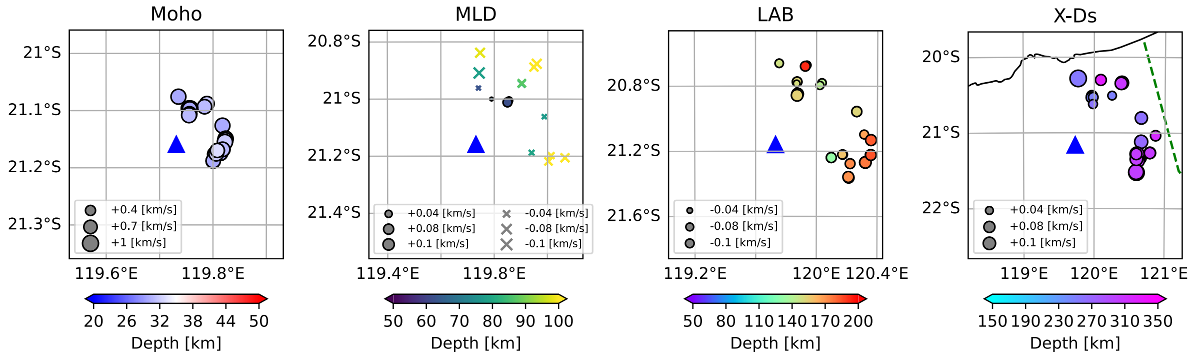

(b) IU.NWAO

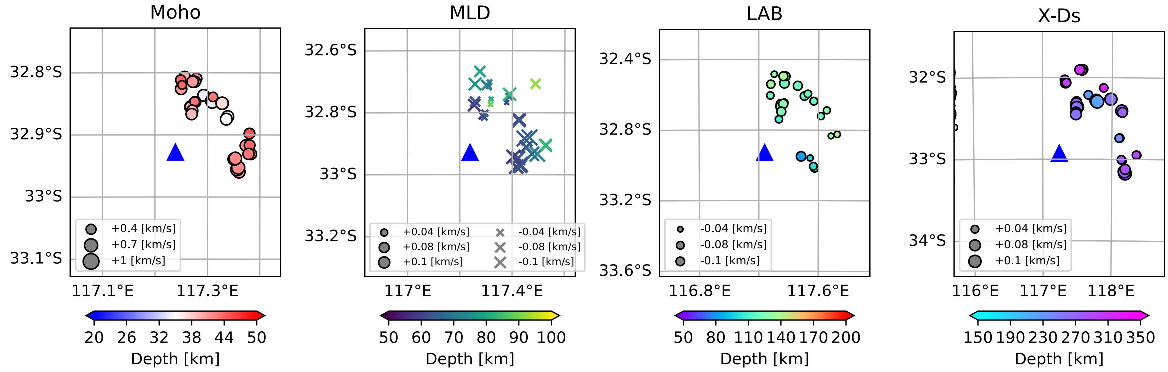

(c) II.WRAB

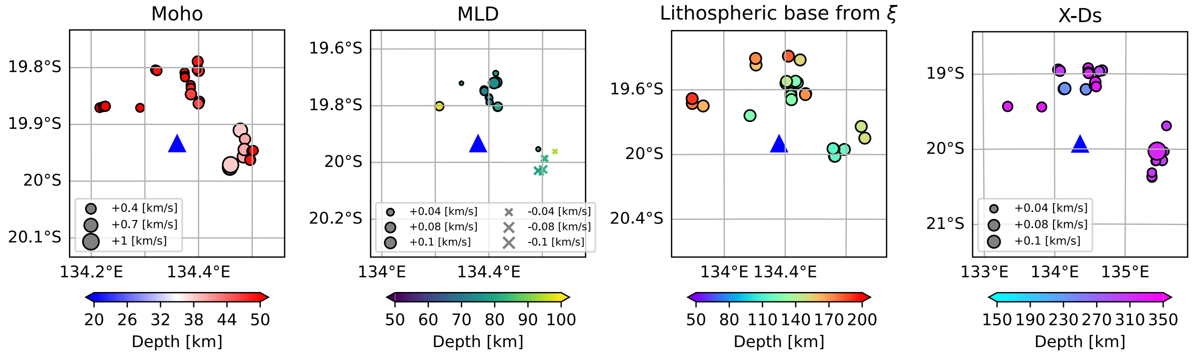

Figure 11: Same as Figure 9, but for three cratonic stations where MLDs have been observed: (a) IU.MBWA, (b) IU.NWAO, and (c) II.WRAB. CP maps for MLDs are added to the mid-left panel in all stations. Note that the mid-right panel for (c) II.WRAB represents the lithospheric base derived from an increase of radial anisotropy ξ, for which the circle sizes are constant, unlike other panels. The mid-left panel displays the CPs for MLDs, with circles and crosses indicating negative and positive changes in shear velocity, respectively.

5.2.1. Moho, LAB, and X-Ds in cratonic regions

For the Moho, CP maps at MBWA and NWAO are almost azimuth-independent, but WRAB shows varying depths of about 10 km between the north and east (leftmost panels in Figure 11 (a-c)). This variation, also seen in array-based P-RF studies (Sippl, 2016) and in our P-RF data (Figure 3 and S5), suggests changes in Moho geometry around WRAB.

The LAB or lithospheric base shows clear azimuthal trends, especially at MBWA and WRAB. At MBWA, the CPs for LAB are located at depths of 140–150 km to the north of the station and become deeper, reaching at 170–180 km, to the east (the third panel in Figure 11 (a)), possibly reflecting a structural transition near the tectonic margin

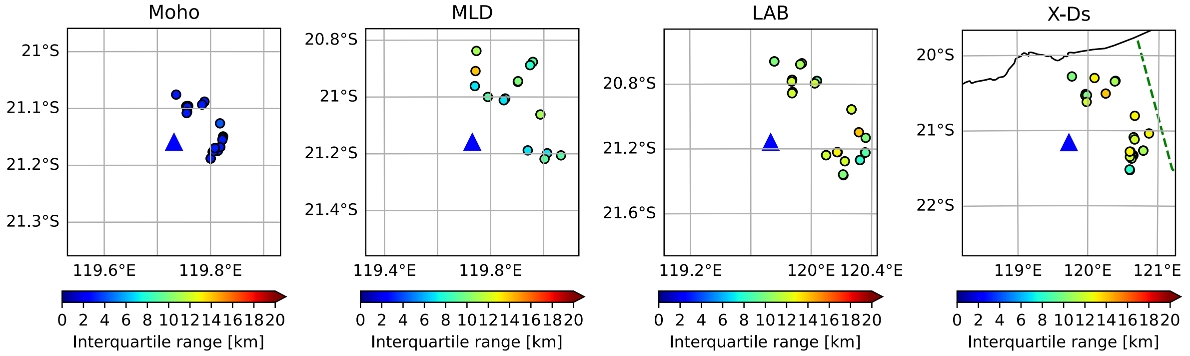
(a) IU.MBWA

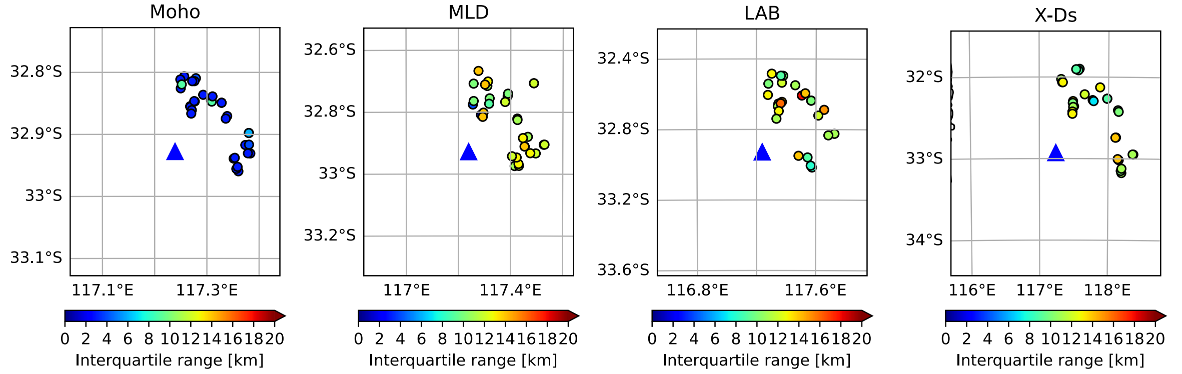
(b) IU.NWAO

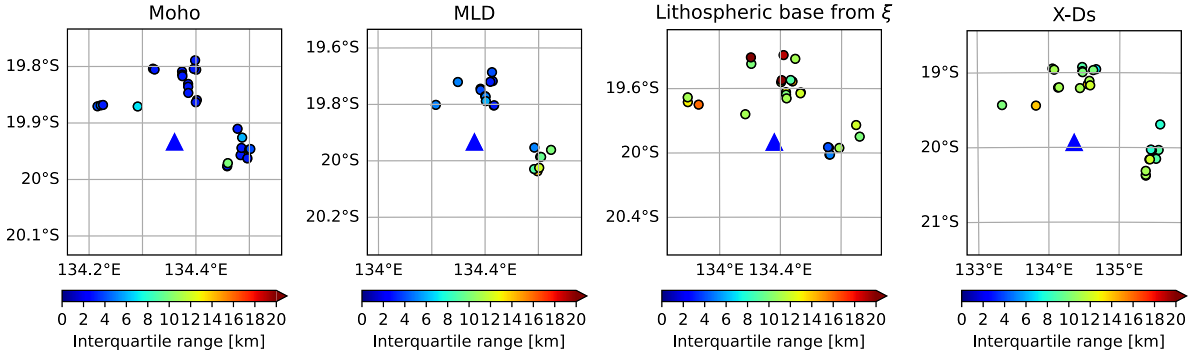
(c) II.WRAB

Figure 12: Same as Figure 10. As in Figure 11, the interquartile ranges of MLDs are shown here.

between the Pilbara craton and the suture zone. At NWAO, the LAB appears to be somewhat deeper to the north of the station (∼ 130 km) than to the east (100–110 km), as shown in Figure 7 (e, f), consistent with previous models (Kennett et al., 2013; Yoshizawa, 2014; Magrini et al., 2023). Comparing the two stations in the WAC, the velocity variations at MBWA appear more pronounced than at NWAO (Figure 11 (a, b)). At WRAB, where lithospheric base depths are inferred from radial anisotropy, the lithospheric thickness varies from 120-140 km in the southeast to about 180 km in the northwest (Figure 11 (c)), consistent with the LAB model from fundamental-mode surface waves (Magrini et al., 2023). The upper limit of the LAT derived from the multimode surface waves (Yoshizawa, 2014) indicates that WRAB is located at the transition between the shallow and deep LAT regions. Our results may reflect such lateral heterogeneity in the upper mantle structure.

The CP maps for X-Ds, associated with positive velocity changes and weaker radial anisotropy, show less azimuthal dependence than the LAB or the lithospheric base at all three stations (right panels in Figure 11). While we did not detect localized X-D variations, CP depths indicate two distinct depths for each station: 260 km and 300–310 km for MBWA, 220 km and 270–290 km for NWAO, and 240 km and 320 km for WRAB. The shallower depth at MBWA is equivalent to the Lehmann discontinuity identified by Taira and Yoshizawa (2020), though we did not observe an interface at 200 km as reported by Drummond et al. (1982). Besides, the deeper interface at 300 km has not been reported previously. At NWAO, the deeper depth matches observations in Revenaugh and Jordan (1991), while the shallower one has not been reported. For WRAB, our CP map for X-Ds cluster below 300 km depths, with a previously unreported discontinuity around 230–240 km (Figure 11 (c)). Earlier studies using P-wave amplitudes and travel times (Hales et al., 1980; Leven, 1985) also suggested discontinuities around 200 km and 325 km beneath the NAC. Some of our X-Ds are consistent with these earlier findings, suggesting multiple interfaces are present. Extended spatial mapping with more stations will be essential for further investigating the X-Ds (or Lehmann discontinuity).

5.2.2. *MLDs in cratonic regions*

The CPs of MLDs beneath MBWA and NWAO show shear wave speed reductions at multiple depths within the lithosphere (Figure 11), consistent with earlier studies (Ford et al., 2010; Sun et al., 2018; Taira and Yoshizawa, 2020; Birkey et al., 2021). At MBWA, despite the smaller number of detections in the inversion results, the CP maps for MLDs (Figure 11) indicate shear wave speed jumps at 60 km depth, possibly corresponding to shallower positive S-RF phases reported by Birkey et al. (2021).

In contrast, MLDs at WRAB exhibit unique characteristics (mid-left panel in Figure 11 (c)). To the east of WRAB, shear wave speed reductions at 80–90 km are consistent with negative MLDs detected in S-RF and joint inversion studies (Ford et al., 2010; Birkey et al., 2021; Taira and Yoshizawa, 2020). The earlier inversion study by Taira and Yoshizawa (2020), which mainly used events from the Tonga-Kermadec Trench, identified negative MLDs at 80 km depth, which matches our results in the east of WRAB. To the north of WRAB, however, we observe increased S-wave speeds at 70–80 km depth, consistent with classical studies that detected a positive velocity step at around 75 km in the NAC using events from the Banda Sea, equivalent to the Hales discontinuity (Hales et al., 1980). This observation contrasts with the negative MLDs found in S-RFs for the northern piercing points (Ford et al., 2010), possibly reflecting intrinsic differences between P-RFs and S-RFs, such as in conversion points, incident angles, and wavelengths.

An alternative explanation may involve vertical variations in azimuthal anisotropy. Selway et al. (2015) suggested MLDs in RFs could result from azimuthal anisotropic layering through simple forward modeling of RFs. Similarly, Chen et al. (2021) and Birkey and Ford (2023) discussed the link between the depths of MLDs and vertical changes in azimuthal anisotropy, using azimuth-dependent radial and transverse P-RFs in Australian cratons. Around WRAB, layered azimuthal anisotropy has been imaged by surface wave tomography (Simons et al., 2002; Debayle et al., 2005; de Laat et al., 2023). Incorporating azimuthal anisotropy in our joint inversion methods of P-RFs and SWDs will provide additional constraints on the nature of MLDs, though it is beyond the scope of the current study.

Although our dataset does not involve azimuthal anisotropy, it includes multimode Love and Rayleigh wave dispersions in addition to P-RFs, allowing us to analyze radial anisotropy across MLDs. Yoshizawa and Kennett (2015) compared their radially anisotropic S-wave model derived from the multimode SWDs and S-RFs by Ford et al. (2010), suggesting that the MLDs may be linked to the vertical changes (weakening) of radial anisotropy. Subsequent studies proposed that MLDs may involve multiple interfaces (Sun et al., 2018; Taira and Yoshizawa, 2020; Chen et al., 2021; Birkey et al., 2021), though the relationship between MLDs and radial anisotropy ξ remains unclear.

To investigate this point, we examined the vertical gradient signs of ξ across MLDs in Figure 13, excluding CPs with change smaller than 1 %. The resultant CP maps in (Figure 13) reveal distinct patterns by station. At MBWA, shallower MLDs show a decrease in ξ, while deeper interfaces indicate increasing anisotropy (Figure 13 (a)). At NWAO, shallow eastern MLDs ($\approx$ 60 km) show increasing ξ, while deeper MLDs (70–80 km) show a decrease (Figure 13 (b)). At WRAB, azimuthal dependency aligns with S-wave speed changes (Figure 13 (c)): positive speed changes coincide with weakened radial anisotropy and vice versa. Although the localized CPs do not fully clarify the nature of multiple MLDs, these new findings may contribute to understanding the origins of MLDs.

6. Discussion

To validate our approach of estimating localized conversion depths using azimuth-dependent radial P-RFs, we plot the estimated conversion points at CTAO, CAN, and WRAB on the E-W cross sections of the tomography model from

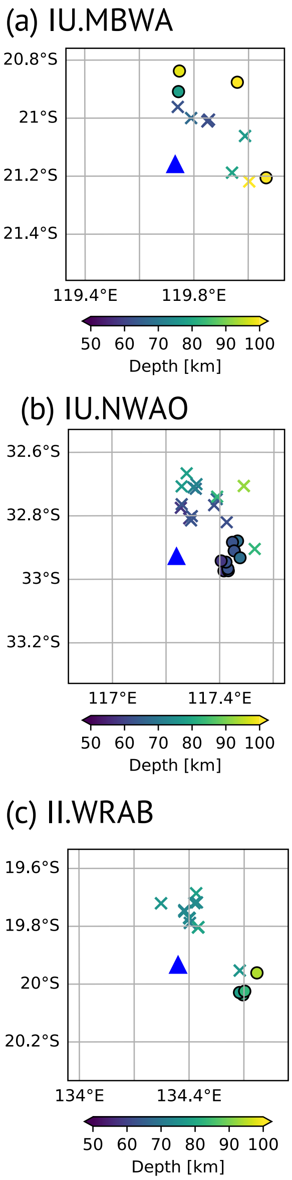

Figure 13: The vertical change in radial anisotropy (> 1%) across the MLDs at (a) IU.MBWA, (b) IU.NWAO, and (c) II.WRAB. Blue triangles represent station locations. Colored symbols denote the conversion points, with color indicating depth. Circles and crosses denote positive and negative changes in radial anisotropy ξ with depth, respectively.

Yoshizawa (2014) in Figure 14. Since the employed events are mostly distributed in a limited range from the northwest to the east of Australia, we lack CP samples in the south of all stations. We selected three stations (CTAO, CAN, and WRAB), for which nearly 180° in back-azimuth is covered, excluding MBWA and NWAO to avoid biases due to very limited azimuthal coverage (about 90°).

Figure 14 compares our estimated CPs for MLDs, LAB, and X-Ds with the surface-wave tomography models (Yoshizawa, 2014) with depth uncertainties estimated from the IQRs for each discontinuity. Projected conversion points (CPs) are located within 70 km of each station. The background contours display isotropic S-wave speed in the top panels and radial anisotropy in the bottom.

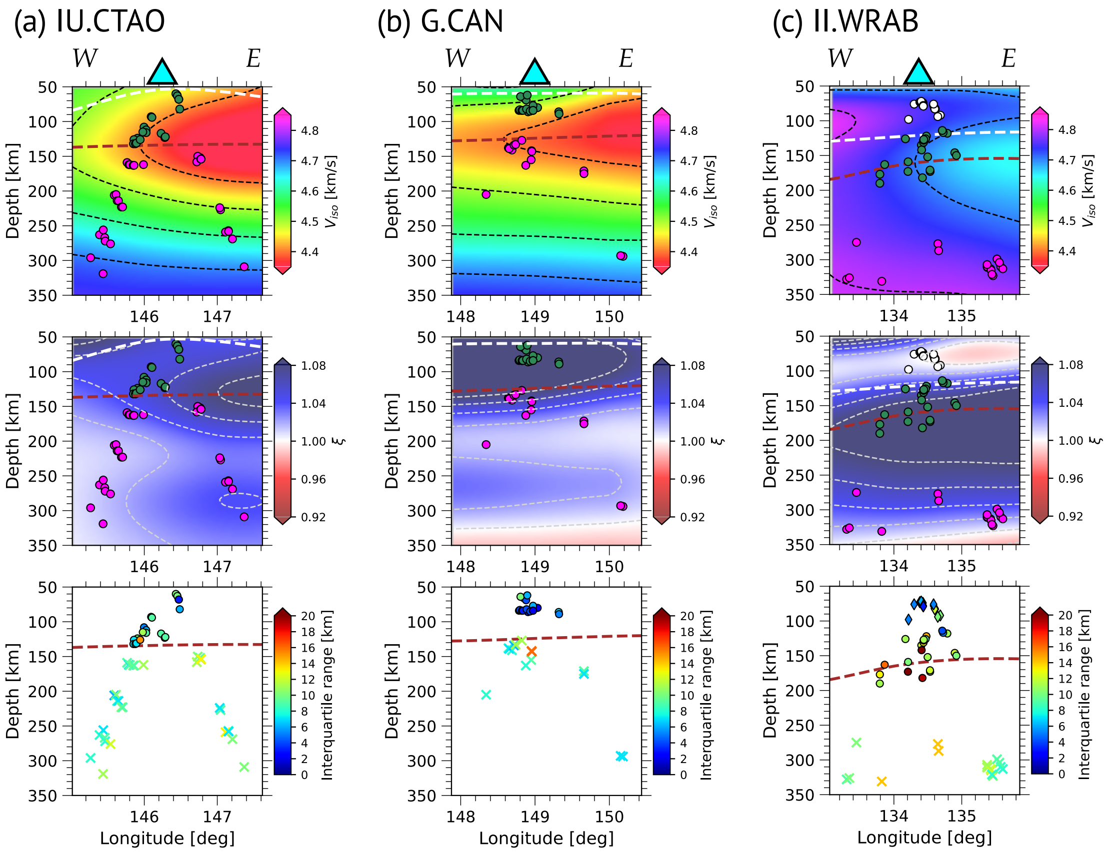

Figure 14: Comparison of conversion points from this study with E-W cross-section of the isotropic S-wave speed (top panels) and radial anisotropy (middle panels) models by Yoshizawa (2014), and interquartile ranges (bottom panels): (a) IU.CTAO, (b) G.CAN, and (c) II.WRAB. Cyan triangles show station locations. White and red thick dashed lines indicate the upper and lower bounds of the LAT (Yoshizawa, 2014). Black and white thin dashed lines represent shear wave speed contours of 0.1 km/s and the radial anisotropy of 0.04. White, green, and magenta dots denote conversion points for the MLDs, lithospheric base, and X-Ds, respectively. For bottom panels, circles, crosses, and diamonds represent IQR-based uncertainties for the LAB (or lithospheric base), X-Ds, and MLDs, respectively.

The LAB (or the lithospheric base) CPs are located at the transition to a relatively lower-velocity zone, particularly evident at CTAO and CAN (Figure 14). Beneath CTAO, our estimates closely match the lateral change in the low-velocity zone. For WRAB, the lithospheric base is situated within a low-velocity zone relative to the surrounding area, supporting our definition based on radial anisotropy can be reasonable in the southern NAC. These LAB CP depths generally align with the regions of intense radial anisotropy, reflecting the asthenospheric shear flow. Thus, our local CP maps effectively capture the lateral variations of lithospheric thickness.

The X-D CPs, associated with S-wave velocity increases, coincide with weakened radial anisotropy, which is consistent with characteristics of the Lehmann discontinuity (L-D) as previously described (e.g., Gaherty and Jordan, 1995; Thybo, 2006; Calò et al., 2016; Taira and Yoshizawa, 2020), suggesting a transition from dislocation to diffusion creep across the L-D (Karato, 1992). Although our CPs for X-Ds are observed at multiple depths with varied agreement to previous studies, they likely correspond to the L-D as the base of the anisotropic layer (Gaherty and Jordan, 1995; Karato, 1992). Furthermore, our detected X-D depths form some clusters at specific depths, consistent with earlier studies (Hales et al., 1980; Leven, 1985; Revenaugh and Jordan, 1991; Taira and Yoshizawa, 2020), suggesting multiple interfaces below the LAB. These CPs contribute to understanding large-scale X-D distributions, which could further illuminate the origins of these interfaces when combined with other geophysical insights, such as the phase transitions of constituent minerals.

In Figure 14 (c) at WRAB, MLDs are observed at multiple depths from 60–90 km, where the S-wave velocity is notably high (≈ 4.75 km/s), with weak velocity changes in the uppermost mantle beneath the station. The tomographic S-wave model in Figure 14 (c) shows a positive velocity gradient downward in these depths, matching the MLDs north of WRAB (around 70 km depth), characterized by positive velocity jumps in our observation (Figure 11 (c)). In contrast, the MLDs east of WRAB (around 80 km depth) appear near a relatively lower-velocity zone extending to the LAT, likely corresponding to negative S-RF peaks.

Some earlier S-RF studies have suggested negative peaks at MLD depths (Birkey et al., 2021), suggesting shear velocity reduction, where positive velocity jumps are detected in the north of WARB in our study. One possible explanation is the influence of azimuthal anisotropy, which our current study did not consider but can be a topic of future work. In addition, MLDs identified in both S-RF studies and our model may be related to reductions in radial anisotropy within the lithosphere (Figures 13 and 14; Yoshizawa and Kennett, 2015; Taira and Yoshizawa, 2020). Recent azimuthal anisotropy model also indicates rapid fast-axis changes at the MLD depths (de Laat et al., 2023), suggesting that some MLDs may reflect changes in anisotropic properties, which can also be evident from the azimuth-dependent transverse P-RFs (Birkey and Ford, 2023).

Moreover, the MLD characteristics appear to vary by tectonic province, likely due to distinct ancient tectonic events in each craton. Applying our joint inversion approach to more stations across Australia will allow us to better map MLD distribution and elastic properties, providing further insights into these regional differences.

7. Conclusions

In this study, we introduced a new approach using azimuth-dependent P-wave receiver functions (P-RFs) in the framework of joint Bayesian inversions with multimode surface wave data. Azimuthal variations in P-RFs generally indicate lateral changes in seismic interfaces or anisotropic layering beneath a station. Based on the posterior of local 1-D profiles, we estimated the major seismic interfaces in the upper mantle, which led to the construction of conversion point maps for each discontinuity.

Through analysis of five permanent stations, we identified some notable characteristics of upper mantle discontinuities beneath Australia, which can be summarized as follows:

1. Beneath CTAO in northeastern Australia, the lithosphere-asthenosphere boundary (LAB) deepens sharply from ~70 km in the east to 120-130 km toward the west and north. In contrast, the LAB under CAN is nearly flat at ~80 km.
2. In the stable craton of western Australia, the LAB depth varies laterally, though more gradually than in the eastern Phanerozoic region.
3. Australian X-discontinuities (X-Ds) beneath the LAB appear at three to four distinct depths, indicating multiple interfaces with weakened radial anisotropy.
4. MLDs consist of multiple interfaces at varying lithospheric depths, with different elastic properties by location. In particular, MLDs beneath WRAB include shallower positive discontinuities previously unreported in Australian S-RF studies.

Due to the limitations of our data set to five permanent stations, the spatial distributions of upper mantle discontinuities remain unconstrained. In future work, we plan to incorporate all the available permanent and temporary stations across Australia to construct a comprehensive map of the lithosphere, MLDs, and X-discontinuities beneath the LAB using our approach proposed in this study. This mapping will clarify continental-wide distributions and the seismological nature of each discontinuity, deepening our understanding of Australia's ancient and present tectonics.

Acknowledgments

We thank the editor, Ana Ferreira, and two anonymous reviewers for constructive comments to improve the original manuscript. We downloaded all seismograms used in this study from the IRIS Data Management Center (https://ds.iris.edu/ds/nodes/dmc/). This study was partly supported by JST SPRING grant number JPMJSP2119 to KT and JSPS KAKENHI (grant number 24KJ0294 to KT; 20K04096 and 23K03539 to KY). We used ObsPy (Beyreuther et al., 2010) for downloading and analyzing all seismic waveform data. We used matplotlib (Hunter, 2007), cartopy (Office, 2010), Generic Mapping Tools (Wessel et al., 2019), and PyGMT (Uieda et al., 2021) to create figures. We thank Toru Taira for sharing his original trans-dimensional Bayesian inversion codes, which were helpful during the development of methods in this study. This study was partly achieved through the use of the supercomputer system at the information initiative center, Hokkaido University.

Data Availability

All the seismograms used in this study can be available from the IRIS Data Management Center (https://ds.iris.edu/ds/nodes/d

CRediT authorship contribution statement

Kotaro Tarumi: Conceptualization, Data curation, Methodology, Formal analysis, Funding acquisition, Investigation, Visualization, Software, Writing - Original draft. **Kazunori Yoshizawa:** Conceptualization, Data curation, Methodology, Funding acquisition, Investigation, Supervision, Project Administration, Writing – review and editing.

References

Abt, D.L., Fischer, K.M., French, S.W., Ford, H.A., Yuan, H., Romanowicz, B., 2010. North American lithospheric discontinuity structure imaged by Ps and Sp receiver functions. Journal of Geophysical Research: Solid Earth (1978–2012) 115. doi:10.1029/2009jb006914.

Ai, S., Akuhara, T., Morishige, M., Yoshizawa, K., Shinohara, M., Nakahigashi, K., 2023. Layered Evolution of the Oceanic Lithosphere Beneath the Japan Basin, the Sea of Japan. Journal of Geophysical Research: Solid Earth 128. doi:10.1029/2022jb025581.

Akuhara, T., Nakahigashi, K., Shinohara, M., Yamada, T., Shiobara, H., Yamashita, Y., Mochizuki, K., Uehira, K., 2021. Lithosphere–asthenosphere boundary beneath the Sea of Japan from transdimensional inversion of S-receiver functions. Earth, Planets and Space 73, 171. doi:10.1186/s40623-021-01501-5.

Argus, D.F., Gordon, R.G., DeMets, C., 2011. Geologically current motion of 56 plates relative to the no-net-rotation reference frame. Geochemistry, Geophysics, Geosystems 12, n/a–n/a. doi:10.1029/2011gc003751.

Beyreuther, M., Barsch, R., Krischer, L., Megies, T., Behr, Y., Wassermann, J., 2010. ObsPy: A Python Toolbox for Seismology. Seismological Research Letters 81, 530–533. doi:10.1785/gssrl.81.3.530.

Bianchi, I., Park, J., Agostinetti, N.P., Levin, V., 2010. Mapping seismic anisotropy using harmonic decomposition of receiver functions: An application to Northern Apennines, Italy. Journal of Geophysical Research: Solid Earth 115. doi:10.1029/2009jb007061.

Birkey, A., Ford, H.A., 2023. Anisotropic structure of the Australian continent. Frontiers in Earth Science 10, 1055480. doi:10.3389/feart.2022.1055480.

Birkey, A., Ford, H.A., Dabney, P., Goldhagen, G., 2021. The Lithospheric Architecture of Australia From Seismic Receiver Functions. Journal of Geophysical Research: Solid Earth 126. doi:10.1029/2020jb020999.

Bodin, T., Leiva, J., Romanowicz, B., Maupin, V., Yuan, H., 2016. Imaging anisotropic layering with Bayesian inversion of multiple data types. Geophysical Journal International 206, 605–629. doi:10.1093/gji/ggw124.

Bodin, T., Sambridge, M., Tkalčić, H., Arroucau, P., Gallagher, K., Rawlinson, N., 2012. Transdimensional inversion of receiver functions and surface wave dispersion. Journal of Geophysical Research: Solid Earth (1978–2012) 117, n/a–n/a. doi:10.1029/2011jb008560.

Bodin, T., Yuan, H., Romanowicz, B., 2014. Inversion of receiver functions without deconvolution—application to the Indian craton. Geophysical Journal International 196, 1025–1033. doi:10.1093/gji/ggt431.

Calò, M., Bodin, T., Romanowicz, B., 2016. Layered structure in the upper mantle across North America from joint inversion of long and short period seismic data. Earth and Planetary Science Letters 449, 164–175. doi:10.1016/j.epsl.2016.05.054.

Chen, X., Levin, V., Yuan, H., Klaser, M., Li, Y., 2021. Seismic Anisotropic Layering in the Yilgarn and Superior Cratonic Lithosphere. Journal of Geophysical Research: Solid Earth 126. doi:10.1029/2020jb021575.

Cheng, C., Bodin, T., Tauzin, B., Allen, R.M., 2017. Cascadia subduction slab heterogeneity revealed by three-dimensional receiver function Kirchhoff migration. Geophysical Research Letters 44, 694–701. doi:10.1002/2016gl072142.

Davies, D.R., Rawlinson, N., Iaffaldano, G., Campbell, I.H., 2015. Lithospheric controls on magma composition along Earth's longest continental hotspot track. Nature 525, 511–514. doi:10.1038/nature14903.

Debayle, E., Kennett, B., Priestley, K., 2005. Global azimuthal seismic anisotropy and the unique plate-motion deformation of Australia. Nature 433, 509–512. doi:10.1038/nature03247.

Debayle, E., Kennett, B.L.N., 2000. The Australian continental upper mantle: Structure and deformation inferred from surface waves. Journal of Geophysical Research: Solid Earth 105, 25423–25450. doi:10.1029/2000jb900212.

de Laat, J.I., Lebedev, S., Celli, N.L., Bonadio, R., Chagas de Melo, B., Rawlinson, N., 2023. Structure and evolution of the Australian plate and underlying upper mantle from waveform tomography with massive data sets. Geophysical Journal International 234, 153–189. doi:10.1093/gji/ggad062.

Drummond, B.J., Muirhead, K.J., Hales, A.L., 1982. Evidence for a seismic discontinuity near 200km depth under a continental margin. Geophysical Journal International 70, 67–77. doi:10.1111/j.1365-246x.1982.tb06392.x.

Dziewonski, A.M., Anderson, D.L., 1981. Preliminary reference Earth model. Physics of the Earth and Planetary Interiors 25, 297–356. doi:10.1016/0031-9201(81)90046-7.

Dziewonski, A.M., Chou, T., Woodhouse, J.H., 1981. Determination of earthquake source parameters from waveform data for studies of global and regional seismicity. Journal of Geophysical Research: Solid Earth 86, 2825–2852. doi:10.1029/jb086ib04p02825.

Ekström, G., Nettles, M., Dziewoński, A., 2012. The global CMT project 2004–2010: Centroid-moment tensors for 13,017 earthquakes. Physics of the Earth and Planetary Interiors 200, 1–9. doi:10.1016/j.pepi.2012.04.002.

Fischer, K.M., Ford, H.A., Abt, D.L., Rychert, C.A., 2010. The Lithosphere-Asthenosphere Boundary. Annual Review of Earth and Planetary Sciences 38, 551–575. doi:`10.1146/annurev-earth-040809-152438`.

Fischer, K.M., Rychert, C.A., Dalton, C.A., Miller, M.S., Beghein, C., Schutt, D.L., 2020. A comparison of oceanic and continental mantle lithosphere. Physics of the Earth and Planetary Interiors 309, 106600. doi:`10.1016/j.pepi.2020.106600`.

Fishwick, S., Heintz, M., Kennett, B.L.N., Reading, A.M., Yoshizawa, K., 2008. Steps in lithospheric thickness within eastern Australia, evidence from surface wave tomography. Tectonics 27, n/a–n/a. doi:`10.1029/2007tc002116`.

Ford, H.A., Fischer, K.M., Abt, D.L., Rychert, C.A., Elkins-Tanton, L.T., 2010. The lithosphere–asthenosphere boundary and cratonic lithospheric layering beneath Australia from Sp wave imaging. Earth and Planetary Science Letters 300, 299–310. doi:`10.1016/j.epsl.2010.10.007`.

Ford, H.A., Long, M.D., Wirth, E.A., 2016. Midlithospheric discontinuities and complex anisotropic layering in the mantle lithosphere beneath the Wyoming and Superior Provinces. Journal of Geophysical Research: Solid Earth 121, 6675–6697. doi:`10.1002/2016jb012978`.

Frederiksen, A.W., Bostock, M.G., 2000. Modelling teleseismic waves in dipping anisotropic structures. Geophysical Journal International 141, 401–412. doi:`10.1046/j.1365-246x.2000.00090.x`.

Frederiksen, A.W., Folsom, H., Zandt, G., 2003. Neighbourhood inversion of teleseismic Ps conversions for anisotropy and layer dip. Geophysical Journal International 155, 200–212. doi:`10.1046/j.1365-246x.2003.02043.x`.

Gaherty, J.B., Jordan, T.H., 1995. Lehmann Discontinuity as the Base of an Anisotropic Layer Beneath Continents. Science 268, 1468–1471. doi:`10.1126/science.268.5216.1468`.

Gilbert, H., Beck, S., Zandt, G., 2006. Lithospheric and upper mantle structure of central Chile and Argentina. Geophysical Journal International 165, 383–398. doi:`10.1111/j.1365-246x.2006.02867.x`.

Green, P.J., 1995. Reversible jump Markov chain Monte Carlo computation and Bayesian model determination. Biometrika 82, 711–732. doi:`10.1093/biomet/82.4.711`.

Hales, A., Muirhead, K., Rynn, J., 1980. A compressional velocity distribution for the upper mantle. Tectonophysics 63, 309–348. doi:`10.1016/0040-1951(80)90119-5`.

Haskell, N.A., 1962. Crustal reflection of plane P and SV waves. Journal of Geophysical Research 67, 4751–4768. doi:`10.1029/jz067i012p04751`.

Hastings, W.K., 1970. Monte Carlo sampling methods using Markov chains and their applications. Biometrika 57, 97–109. doi:`10.1093/biomet/57.1.97`.

Hunter, J.D., 2007. Matplotlib: A 2D Graphics Environment. Computing in Science & Engineering 9, 90–95. doi:`10.1109/mcse.2007.55`.

Julià, J., Ammon, C.J., Herrmann, R.B., Correig, A.M., 2000. Joint inversion of receiver function and surface wave dispersion observations. Geophysical Journal International 143, 99–112. doi:`10.1046/j.1365-246x.2000.00217.x`.

Karato, S., 1992. On the Lehmann discontinuity. Geophysical Research Letters 19, 2255–2258. doi:`10.1029/92gl02603`.

Kennett, B., Yoshizawa, K., Furumura, T., 2017. Interactions of multi-scale heterogeneity in the lithosphere: Australia. Tectonophysics 717, 193–213. URL: `http://www.sciencedirect.com/science/article/pii/S0040195117302913`, doi:`10.1016/j.tecto.2017.07.009`.

Kennett, B.L.N., Engdahl, E.R., Buland, R., 1995. Constraints on seismic velocities in the Earth from traveltimes. Geophysical Journal International 122, 108–124. doi:`10.1111/j.1365-246x.1995.tb03540.x`.

Kennett, B.L.N., Fichtner, A., Fishwick, S., Yoshizawa, K., 2013. Australian Seismological Reference Model (AuSREM): mantle component. Geophysical Journal International 192, 871–887. doi:`10.1093/gji/ggs065`.

Kennett, B.L.N., Gorbatov, A., Yuan, H., Agrawal, S., Murdie, R., Doublier, M.P., Eakin, C.M., Miller, M.S., Zhao, L., Czarnota, K., O'Donnell, J.P., Dentith, M., Gessner, K., 2023. Refining the Moho across the Australian continent. Geophysical Journal International 233, 1863–1877. doi:`10.1093/gji/ggad035`.

Kennett, B.L.N., Salmon, M., Saygin, E., Group, A.W., 2011. AusMoho: the variation of Moho depth in Australia. Geophysical Journal International 187, 946–958. doi:`10.1111/j.1365-246x.2011.05194.x`.

Kennett, B.L.N., Sippl, C., 2018. Lithospheric discontinuities in Central Australia. Tectonophysics 744, 10–22. doi:`10.1016/j.tecto.2018.06.008`.

Kim, H., Kawakatsu, H., Akuhara, T., Shinohara, M., Shiobara, H., Sugioka, H., Takagi, R., 2021. Receiver Function Imaging of the Amphibious NE Japan Subduction Zone—Effects of Low-Velocity Sediment Layer. Journal of Geophysical Research: Solid Earth 126. doi:`10.1029/2021jb021918`.

Kim, S., Dettmer, J., Rhie, J., Tkalčić, H., 2016. Highly efficient Bayesian joint inversion for receiver-based data and its application to lithospheric structure beneath the southern Korean Peninsula. Geophysical Journal International 206, 328–344. doi:`10.1093/gji/ggw149`.

Kind, R., Mooney, W.D., Yuan, X., 2020. New insights into the structural elements of the upper mantle beneath the contiguous United States from S-to-P converted seismic waves. Geophysical Journal International doi:`10.1093/gji/ggaa203`.

Kind, R., Yuan, X., 2011. Seismic, Receiver Function Technique, Springer Netherlands, Dordrecht, pp. 1258–1269. URL: `https://doi.org/10.1007/978-90-481-8702-7_12`, doi:`10.1007/978-90-481-8702-7\_12`.

Kind, R., Yuan, X., Kumar, P., 2012. Seismic receiver functions and the lithosphere–asthenosphere boundary. Tectonophysics 536, 25–43. doi:`10.1016/j.tecto.2012.03.005`.

Kumar, P., Kawakatsu, H., Shinohara, M., Kanazawa, T., Araki, E., Suyehiro, K., 2011. P and S receiver function analysis of seafloor borehole broadband seismic data. Journal of Geophysical Research: Solid Earth 116. doi:`10.1029/2011jb008506`.

Langston, C.A., 1979. Structure under Mount Rainier, Washington, inferred from teleseismic body waves. Journal of Geophysical Research: Solid Earth 84, 4749–4762. doi:`10.1029/jb084ib09p04749`.

Leven, J., 1985. The application of synthetic seismograms to the interpretation of the upper mantle P-wave velocity structure in northern Australia. Physics of the Earth and Planetary Interiors 38, 9–27. doi:`10.1016/0031-9201(85)90119-0`.

Levin, V., Park, J., 1997. P-SH conversions in a flat-layered medium with anisotropy of arbitrary orientation. Geophysical Journal International 131, 253–266. doi:`10.1111/j.1365-246x.1997.tb01220.x`.

Liu, L., Tong, S., Li, S., Qaysi, S., 2020. Sp Receiver-Function Images of African and Arabian Lithosphere: Survey of Newly Available Broadband Data. Seismological Research Letters 91, 1813–1819. doi:`10.1785/0220190311`.

Magrini, F., Kästle, E., Pilia, S., Rawlinson, N., Siena, L., 2023. A New Shear-Velocity Model of Continental Australia Based on Multi-Scale Surface-Wave Tomography. Journal of Geophysical Research: Solid Earth 128. doi:`10.1029/2023jb026688`.

Metropolis, N., Rosenbluth, A.W., Rosenbluth, M.N., Teller, A.H., Teller, E., 1953. Equation of State Calculations by Fast Computing Machines. The Journal of Chemical Physics 21, 1087–1092. doi:`10.1063/1.1699114`.

Myers, J.S., Shaw, R.D., Tyler, I.M., 1996. Tectonic evolution of Proterozoic Australia. Tectonics 15, 1431–1446. doi:`10.1029/96tc02356`.

Nagaya, M., Oda, H., Akazawa, H., Ishise, M., 2008. Receiver Functions of Seismic Waves in Layered Anisotropic Media: Application to the Estimate of Seismic AnisotropyReceiver Functions of Seismic Waves in Layered Anisotropic Media. Bulletin of the Seismological Society of America 98, 2990–3006. doi:`10.1785/0120080130`.

Nagaya, M., Oda, H., Kamimoto, T., 2011. Regional variation in shear-wave polarization anisotropy of the crust in southwest Japan as estimated by splitting analysis of Ps-converted waves on receiver functions. Physics of the Earth and Planetary Interiors 187, 56–65. doi:`10.1016/j.pepi.2011.04.016`.

Nataf, H.C., Ricard, Y., 1996. 3SMAC: an a priori tomographic model of the upper mantle based on geophysical modeling. Physics of the Earth and Planetary Interiors 95, 101–122. doi:`10.1016/0031-9201(95)03105-7`.

Office, M., 2010. Cartopy: a cartographic python library with a Matplotlib interface URL: `https://scitools.org.uk/cartopy`.

Park, J., Levin, V., 2016. Anisotropic shear zones revealed by backazimuthal harmonics of teleseismic receiver functions. Geophysical Journal International 207, 1216–1243. doi:`10.1093/gji/ggw323`.

Plomerová, J., Kouba, D., Babuška, V., 2002. Mapping the lithosphere–asthenosphere boundary through changes in surface-wave anisotropy. Tectonophysics 358, 175–185. doi:`10.1016/s0040-1951(02)00423-7`.

Pugh, S., Jenkins, J., Boyce, A., Cottaar, S., 2021. Global receiver function observations of the X-discontinuity reveal recycled basalt beneath hotspots. Earth and Planetary Science Letters 561, 116813. doi:`10.1016/j.epsl.2021.116813`.

Rein, T., Hannemann, K., Thomas, C., Korn, M., 2020. Location and characteristics of the X-discontinuity beneath SW Morocco and the adjacent shelf area using P-wave receiver functions. Geophysical Journal International 223, 1780–1793. doi:`10.1093/gji/ggaa379`.

Revenaugh, J., Jordan, T.H., 1991. Mantle layering from ScS reverberations: 3. The upper mantle. Journal of Geophysical Research: Solid Earth 96, 19781–19810. doi:`10.1029/91jb01487`.

Rychert, C.A., Fischer, K.M., Rondenay, S., 2005. A sharp lithosphere–asthenosphere boundary imaged beneath eastern North America. Nature 436, 542–545. doi:`10.1038/nature03904`.

Rychert, C.A., Rondenay, S., Fischer, K.M., 2007. P-to-S and S-to-P imaging of a sharp lithosphere-asthenosphere boundary beneath eastern North America. Journal of Geophysical Research: Solid Earth (1978–2012) 112. doi:`10.1029/2006jb004619`.

Saito, M., 1988. DISPER80 : A subroutine package for the calculation of seismic normal mode solutions, Seismological Algorithms, p. 293–319.

Salmon, M., Kennett, B.L.N., Saygin, E., 2013. Australian Seismological Reference Model (AuSREM): crustal component. Geophysical Journal International 192, 190–206. doi:`10.1093/gji/ggs004`.

Sambridge, M., 2014. A Parallel Tempering algorithm for probabilistic sampling and multimodal optimization. Geophysical Journal International 196, 357–374. doi:`10.1093/gji/ggt342`.

Selway, K., Ford, H., Kelemen, P., 2015. The seismic mid-lithosphere discontinuity. Earth and Planetary Science Letters 414, 45–57. doi:`10.1016/j.epsl.2014.12.029`.

Shi, D., Wu, Z., Klemperer, S.L., Zhao, W., Xue, G., Su, H., 2015. Receiver function imaging of crustal suture, steep subduction, and mantle wedge in the eastern India–Tibet continental collision zone. Earth and Planetary Science Letters 414, 6–15. doi:`10.1016/j.epsl.2014.12.055`.

Shibutani, T., Ueno, T., Hirahara, K., 2008. Improvement in the Extended-Time Multitaper Receiver Function Estimation TechniqueShort Note. Bulletin of the Seismological Society of America 98, 812–816. doi:`10.1785/0120070226`.

Shiomi, K., Park, J., 2008. Structural features of the subducting slab beneath the Kii Peninsula, central Japan: Seismic evidence of slab segmentation, dehydration, and anisotropy. Journal of Geophysical Research: Solid Earth 113. doi:`10.1029/2007jb005535`.

Simons, F.J., Hilst, R.D.V.D., Montagner, J., Zielhuis, A., 2002. Multimode Rayleigh wave inversion for heterogeneity and azimuthal anisotropy of the Australian upper mantle. Geophysical Journal International 151, 738–754. doi:`10.1046/j.1365-246x.2002.01787.x`.

Sippl, C., 2016. Moho geometry along a north–south passive seismic transect through Central Australia. Tectonophysics 676, 56–69. doi:`10.1016/j.tecto.2016.03.031`.

Srinu, U., Kumar, P., Haldar, C., Kumar, M.R., Srinagesh, D., Illa, B., 2021. X-Discontinuity Beneath the Indian Shield—Evidence for Remnant Tethyan Oceanic Lithosphere in the Mantle. Journal of Geophysical Research: Solid Earth 126. doi:`10.1029/2021jb021890`.

Sun, W., Fu, L., Saygin, E., Zhao, L., 2018. Insights Into Layering in the Cratonic Lithosphere Beneath Western Australia. Journal of Geophysical Research: Solid Earth 123, 1405–1418. doi:`10.1002/2017jb014904`.

Taira, T., Yoshizawa, K., 2020. Upper-mantle discontinuities beneath Australia from transdimensional Bayesian inversions using multimode surface waves and receiver functions. Geophysical Journal International 223, 2085–2100. URL: `https://doi.org/10.1093/gji/ggaa442`, doi:`10.1093/gji/ggaa442`.

Takagi, R., Nishida, K., 2022. Multimode dispersion measurement of surface waves extracted by multicomponent ambient noise cross-correlation functions. Geophysical Journal International 231, 1196–1220. doi:`10.1093/gji/ggac225`.

Takeuchi, H., Saito, M., 1972. Seismic Surface Waves. Methods in Computational Physics: Advances in Research and Applications 11, 217–295. doi:`10.1016/b978-0-12-460811-5.50010-6`.

Tarumi, K., Yoshizawa, K., 2024. Numerical Sheet for "Station-orientation catalog for Australian broadband seismic stations". URL: `https://doi.org/10.5281/zenodo.13985090`.

Tarumi, K., Yoshizawa, K., 2025. Station-Orientation Catalog for Australian Broadband Seismic Stations. Pure and Applied Geophysics URL: `https://doi.org/10.1007/s00024-025-03827-7`, doi:`10.1007/s00024-025-03827-7`.

Thomson, W.T., 1950. Transmission of Elastic Waves through a Stratified Solid Medium. Journal of Applied Physics 21, 89–93. doi:10.1063/1.1699629.

Thybo, H., 2006. The heterogeneous upper mantle low velocity zone. Tectonophysics 416, 53–79. doi:10.1016/j.tecto.2005.11.021.

Tkalčić, H., Chen, Y., Liu, R., Zhibin, H., Sun, L., Chan, W., 2011. Multistep modelling of teleseismic receiver functions combined with constraints from seismic tomography: crustal structure beneath southeast China. Geophysical Journal International 187, 303–326. doi:10.1111/j.1365-246x.2011.05132.x.

Tkalčić, H., Pasyanos, M.E., Rodgers, A.J., Gök, R., Walter, W.R., Al-Amri, A., 2006. A multistep approach for joint modeling of surface wave dispersion and teleseismic receiver functions: Implications for lithospheric structure of the Arabian Peninsula: MULTISTEP MODELING OF ARABIAN LITHOSPHERE. Journal of Geophysical Research: Solid Earth 111, n/a–n/a. doi:10.1029/2005jb004130.

Tonegawa, T., Hirahara, K., Shibutani, T., 2005. Detailed structure of the upper mantle discontinuities around the Japan subduction zone imaged by receiver function analyses. Earth, Planets and Space 57, 5–14. doi:10.1186/bf03351801.

Uieda, L., Tian, D., Leong, W.J., Jones, M., Schlitzer, W., Toney, L., Grund, M., Yao, J., Magen, Y., Materna, K., Newton, T., Anant, A., Ziebarth, M., Wessel, P., Quinn, J., 2021. PyGMT: A Python interface for the Generic Mapping Tools URL: https://doi.org/10.5281/zenodo.5607255, doi:10.5281/zenodo.5607255. the development of PyGMT has been supported by NSF grants OCE-1558403 and EAR-1948603.

Vinnik, L., Kurnik, E., Farra, V., 2005. Lehmann discontinuity beneath North America: No role for seismic anisotropy. Geophysical Research Letters 32. doi:10.1029/2004gl022333.

Vinnik, L.P., Erduran, M., Oreshin, S.I., Kosarev, G.L., Kutlu, Y.A., Çakir, O., Kiselev, S.G., 2014. Joint inversion of P- and S-receiver functions and dispersion curves of Rayleigh waves: The results for the Central Anatolian Plateau. Izvestiya, Physics of the Solid Earth 50, 622–631. doi:10.1134/s106935131404017x.

Wessel, P., Luis, J.F., Uieda, L., Scharroo, R., Wobbe, F., Smith, W.H.F., Tian, D., 2019. The Generic Mapping Tools Version 6. Geochemistry, Geophysics, Geosystems 20, 5556–5564. doi:10.1029/2019gc008515.

Xu, H., Beghein, C., 2019. Measuring higher mode surface wave dispersion using a transdimensional Bayesian approach. Geophysical Journal International 218, 333–353. doi:10.1093/gji/ggz133.

Xu, H., Beghein, C., Panning, M.P., Drilleau, M., Lognonné, P., Driel, M.v., Ceylan, S., Böse, M., Brinkman, N., Clinton, J., Euchner, F., Giardini, D., Horleston, A., Kawamura, T., Kenda, B., Murdoch, N., Stähler, S., 2021. Measuring Fundamental and Higher Mode Surface Wave Dispersion on Mars From Seismic Waveforms. Earth and Space Science 8. doi:10.1029/2020ea001263.

Yoshida, M., Yoshizawa, K., 2020. Continental Drift with Deep Cratonic Roots. Annual Review of Earth and Planetary Sciences 49, 1–23. doi:10.1146/annurev-earth-091620-113028.

Yoshizawa, K., 2014. Radially anisotropic 3-D shear wave structure of the Australian lithosphere and asthenosphere from multi-mode surface waves. Physics of the Earth and Planetary Interiors 235, 33–48. doi:10.1016/j.pepi.2014.07.008.

Yoshizawa, K., Ekström, G., 2010. Automated multimode phase speed measurements for high-resolution regional-scale tomography: application to North America. Geophysical Journal International 183, 1538–1558. doi:10.1111/j.1365-246x.2010.04814.x.

Yoshizawa, K., Kennett, B.L.N., 2002a. Determination of the influence zone for surface wave paths. Geophysical Journal International 149, 440–453. doi:10.1046/j.1365-246x.2002.01659.x.

Yoshizawa, K., Kennett, B.L.N., 2002b. Non-linear waveform inversion for surface waves with a neighbourhood algorithm—application to multimode dispersion measurements. Geophysical Journal International 149, 118–133. doi:10.1046/j.1365-246x.2002.01634.x.

Yoshizawa, K., Kennett, B.L.N., 2004. Multimode surface wave tomography for the Australian region using a three-stage approach incorporating finite frequency effects. Journal of Geophysical Research: Solid Earth 109. doi:10.1029/2002jb002254.

Yoshizawa, K., Kennett, B.L.N., 2015. The lithosphere-asthenosphere transition and radial anisotropy beneath the Australian continent. Geophysical Research Letters 42, 3839–3846. doi:10.1002/2015gl063845.

Yuan, H., Romanowicz, B., Fischer, K.M., Abt, D., 2011. 3-D shear wave radially and azimuthally anisotropic velocity model of the North American upper mantle. Geophysical Journal International 184, 1237–1260. doi:10.1111/j.1365-246x.2010.04901.x.

Supplementary Material for

Detecting rapid lateral changes of upper mantle discontinuities using azimuth-dependent P-wave receiver functions and multimode surface waves

K. Tarumi[1,*] and K. Yoshizawa[1,2]

[1] Department of Natural History Sciences, Graduate School of Science, Hokkaido University, Sapporo 060-0810, Japan

[2]Department of Earth & Planetary Sciences, Faculty of Science, Hokkaido University, Sapporo 060-0810, Japan.

[*]Corresponding author: tarumi.kotaro.jp@gmail.com

Contents of this file:

Supplementary Texts S1 and S2

- Text S1: Description of the Modified Extended-time Multi-Taper Deconvolution
- Text S2: Validations on the influence of the differences in the spectral estimation method (including descriptions of Figures S7–S9)

Supplementary Figures S1 to S14

- Figure S1: Normalized sensitivity kernels of Rayleigh and Love waves
- Figure S2: Phase speed dispersion data for five stations used in this study.
- Figure S3: Event distributions of each station.
- Figure S4: P-wave receiver functions (P-RFs) in various frequency ranges at CTAO.
- Figure S5: P-RFs (0.03–0.5 Hz) at four stations except for CTAO.

- Figure S6: Reference velocity model used for the inversion analysis.
- Figure S7: Standard deviation of stacked RFs (related to Text S2).
- Figure S8: Assessments of synthetic P-RFs computed from different spectral estimation methods (related to Text S2).
- Figure S9: Synthetic model recovery tests (related to Text S2).
- Figure S10–12: Posterior distributions of hyperparameters and data misfits corresponding to the inversion results shown in Figure 5 (b–d).
- Figure S13: Additional inversion results at CAN.
- Figure S14: Piercing point maps for the five stations.

Supplementary Table S1

- Table S1: Summary of parameters for the random walk used in this study.

Text S1: Description of the Modified Extended-time Multi-Taper Deconvolution

For calculating individual observed RFs, we adopted a modified version of the extended-time multi-taper (EXMT) spectral estimation, based on the method by Shibutani et al. (2008), with a key modification to the damping factor in the spectral division.

In the original formulation by Shibutani et al. (2008), the frequency-domain RF is defined as:

$$RF(\omega) = \frac{\sum_{i=0}^{K-1} H(\omega)\widetilde{U}(\omega)}{\sum_{i=0}^{K-1} U(\omega)\widetilde{U}(\omega) + J^2 \sum_{i=0}^{K-1} N(\omega)\widetilde{N}(\omega)},$$

where ω is the angular frequency, $H(\omega)$, $U(\omega)$, and $N(\omega)$ are the Fourier spectrum of horizontal (radial), vertical, and the pre-signal noise time series, respectively. J is the ratio of the number of multi-tapers between the signal and noise windows (ideally, J=1). The second term in the denominator (i.e., involving the noise spectrum) serves as a damping factor to stabilize the deconvolution.

In this study, to ensure consistency in spectral division between observed and synthetic RFs during the inversion (as discussed in Section 3), we replaced the noise-based damping with a flat-level damping factor (based on 0.1 % of the maximum value of $\sum_{i=0}^{K-1} U(\omega)\widetilde{U}(\omega)$), similar to the one used in the standard water-level method. Thus, the modified RF is computed as:

$$RF(\omega) = \frac{\sum_{i=0}^{K-1} H(\omega)\widetilde{U}(\omega)}{\sum_{i=0}^{K-1} U(\omega)\widetilde{U}(\omega) + DF(\omega)},$$

$$DF(\omega) = \begin{cases} 0.001 \times F, & \left(if\ \sum_{i=0}^{K-1} U(\omega)\widetilde{U}(\omega) < 0.001 \times F\right) \\ & 0,\ (otherwise) \end{cases}$$

$$\text{where } F = \max\left(\sum_{i=0}^{K-1} U(\omega)\widetilde{U}(\omega)\right).$$

This flat-level damping approach provides a stable and consistent spectral division that can be applied uniformly to both observed and synthetic RFs, while avoiding the need to define noise spectra for synthetic Green's functions.

Text S2: Validations on the influence of the differences in the spectral estimation method

As described in the main text, we used different spectral estimation methods for observed and synthetic RFs. To evaluate the potential influence of our methodological strategy, we conducted two validation tests:

S2-1. Synthetic RF modeling using different velocity models (Figures S7 and S8)

We compared P-RFs computed via the water-level (WL) method for a series of velocity models containing a velocity jump at 270 km and a reference P-RF computed using the modified EXMT method described in Text S1. Although small amplitude differences appear around 30-second delay time, they fall within the typical uncertainty range of ± 0.03 inferred from the hierarchical Bayesian inversion process (see Figures S10–S12). In addition, the arrival times of Ps phases remain unchanged, indicating that the estimated discontinuity depths are robust. Furthermore, the amplitude differences arising from the different spectral estimation during the RF processing are much smaller than the uncertainties in the stacked observed RFs (Figure S8), suggesting that the influence of the slight discrepancy in the RF processing is negligible.

S2-2. Joint inversion recovery tests (Figure S9)

To further validate the robustness of our approach, we performed a recovery test using synthetic RF generated with the EXMT method. This RF was treated as the input (“observed”) data after adding Gaussian noise ($\sigma = 0.03$), and then jointly inverted with surface-wave dispersion data using our standard WL-based forward modeling.

As shown in Figure S9, the inversion successfully reproduced the input velocity profile (displayed as the cyan dashed lines) and discontinuity depths, although the radial anisotropy between 200 and 270 km shows a slight deviation that remains within the posterior probability distribution, confirming that the differences in RF processing do not significantly affect the final recovered velocity models.

(a) Rayleigh wave

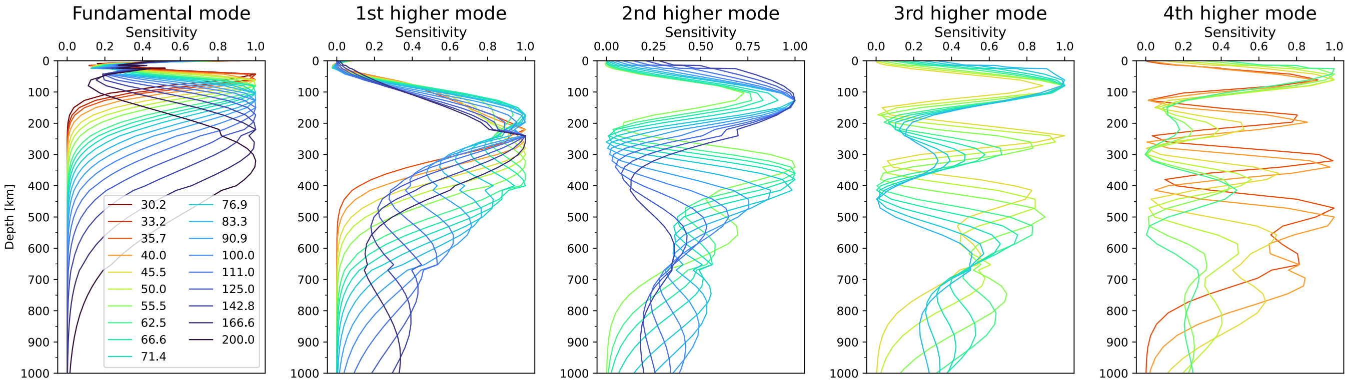

(b) Love wave

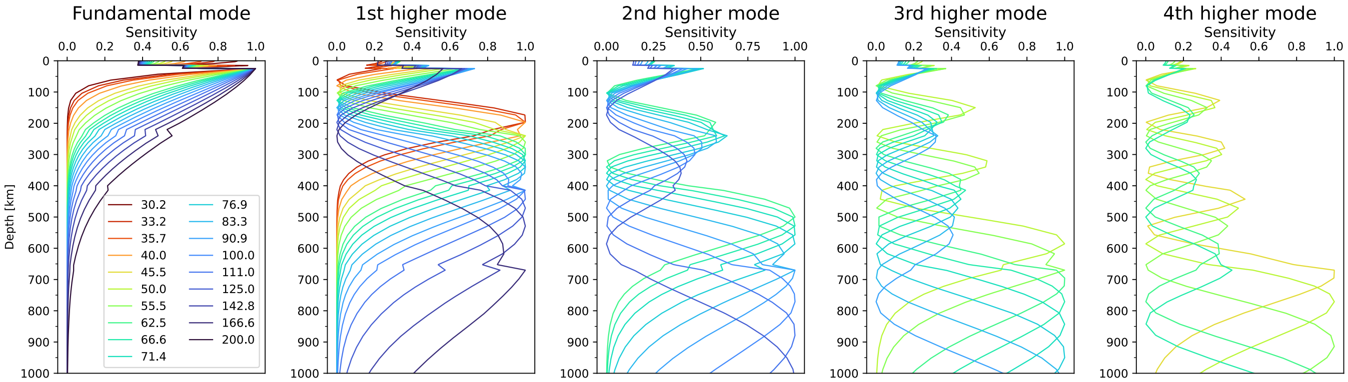

Figure S1. Normalized sensitivity kernels of surface waves for anisotropic PREM (Dziewonski & Anderson, 1981) from the fundamental to the 4th higher mode of (a) Rayleigh waves and (b) Love waves. Line colors indicate the period of surface waves.

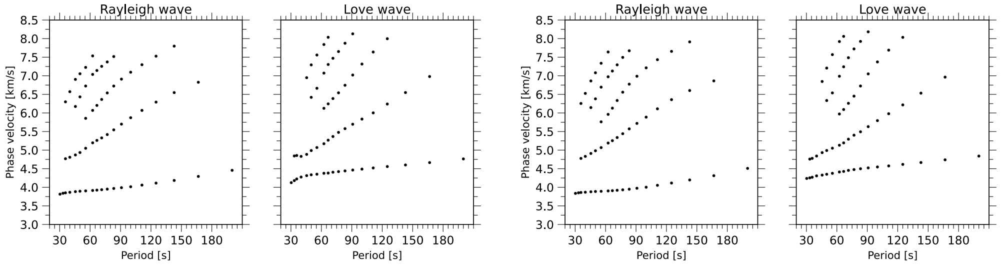

(a) IU.CTAO

(b) G.CAN

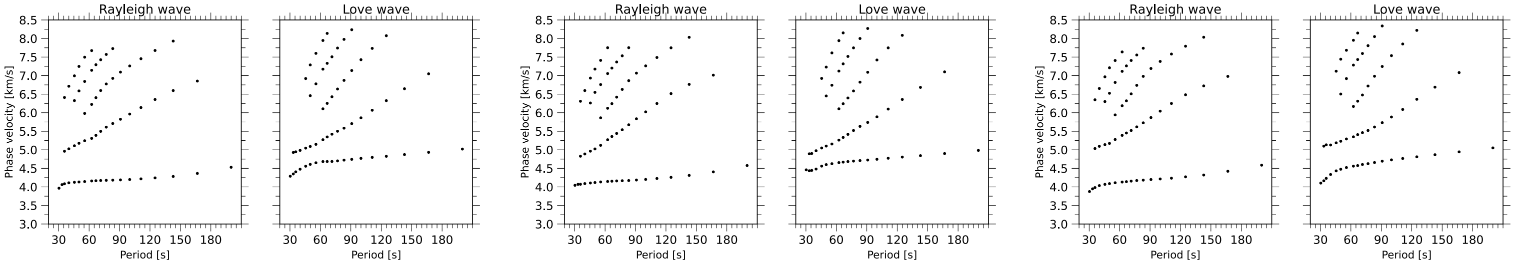

(c) IU.MBWA

(d) IU.NWAO

(e) II.WRAB

Figure S2: Phase speed dispersion data of multimode Rayleigh and Love waves for five stations used in this study (a: IU.CTAO; b: G.CAN; c: IU.MBWA; d: IU.NWAO; e: II.WRAB). These dispersion data are extracted from multimode phase velocity maps by Yoshizawa (2014).

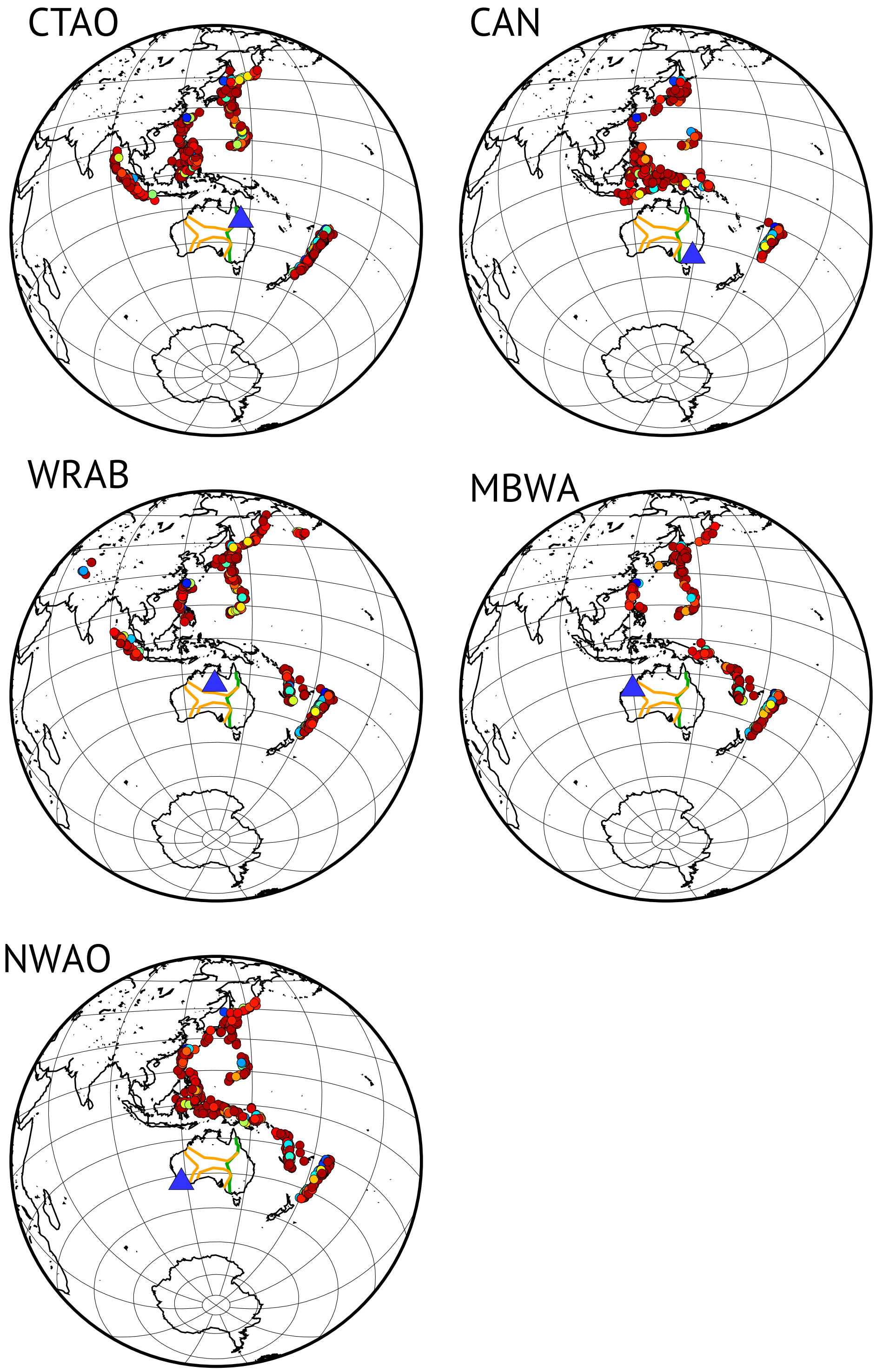

Figure S3: Event distributions for each station used in this study. Notations are the same as Figure 3 (e).

(a) 0.03-0.125 Hz (b) 0.03-0.2 Hz

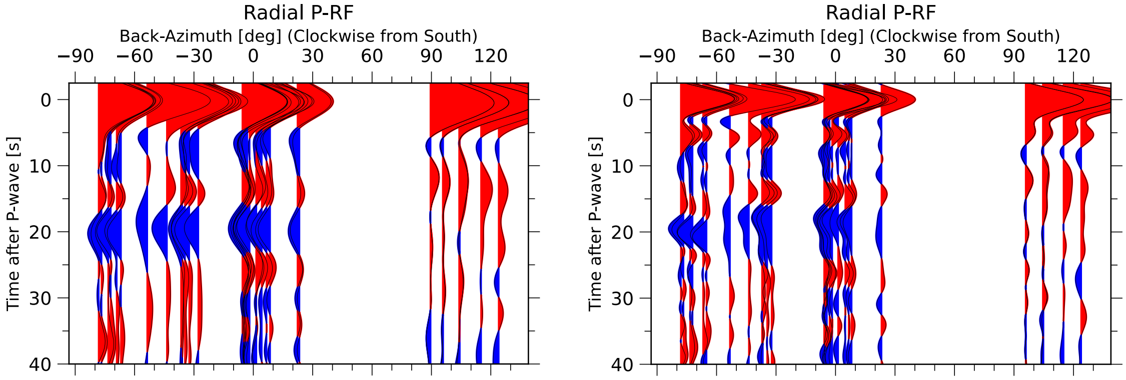

(c) 0.03-0.5 Hz (d) 0.04-1.0 Hz

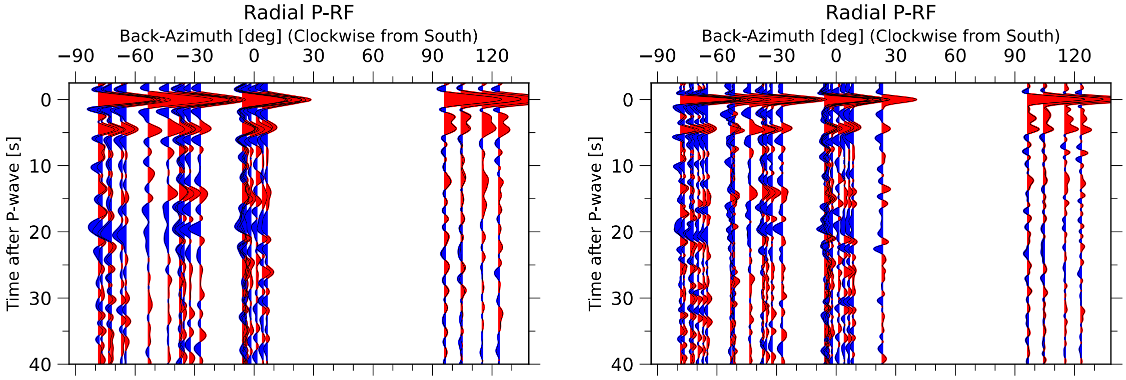

Figure S4: Frequency-dependent P-wave receiver functions (P-RFs) at IU.CTAO for four frequency ranges: (a) 0.03-0.125 Hz, (b) 0.03-0.2 Hz, (c) 0.03-0.5 Hz, and (d) 0.04-1.0 Hz. Red and blue colors represent the positive and negative phases in receiver functions.

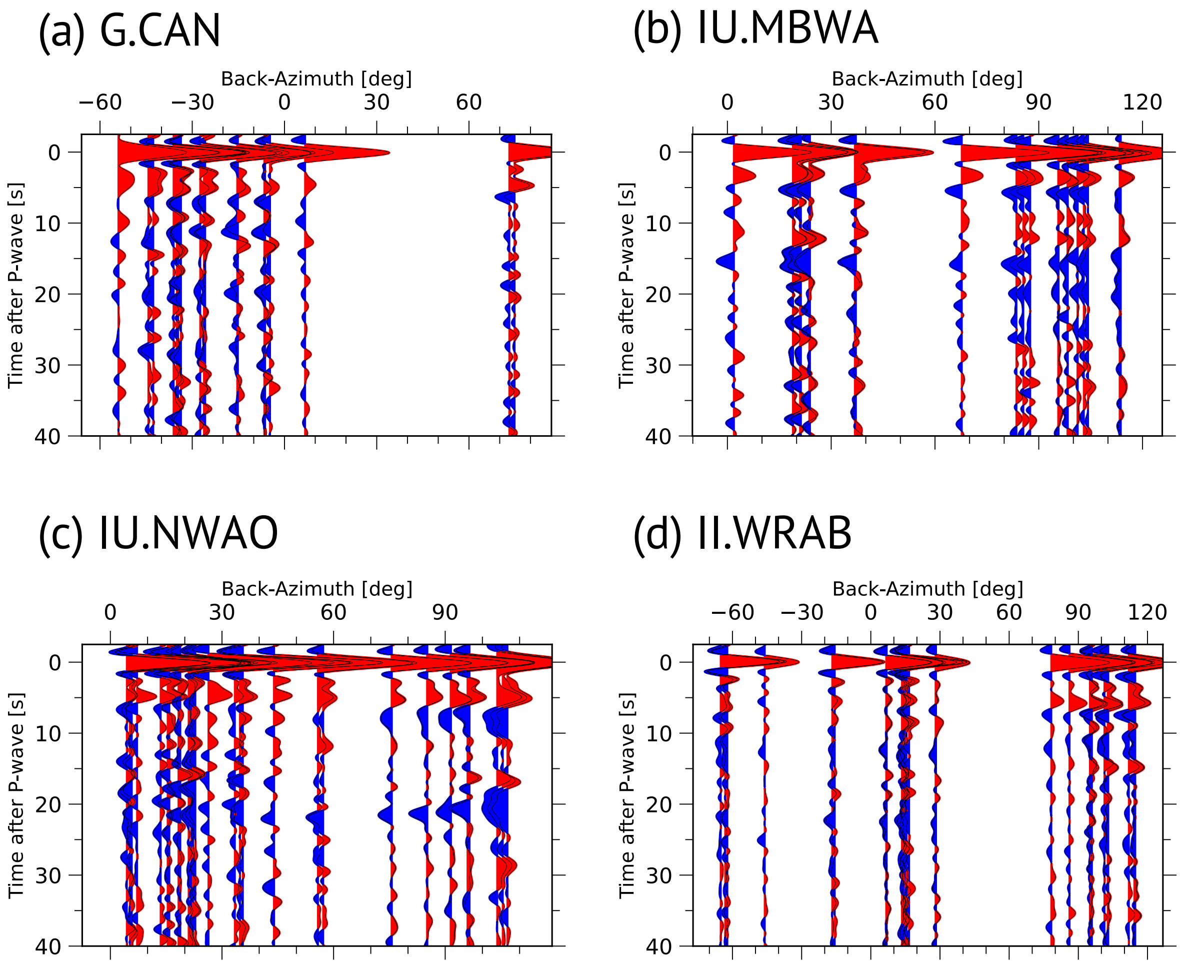

Figure S5: Same as Figure 3 in the main text, but for 0.03-0.5 Hz.

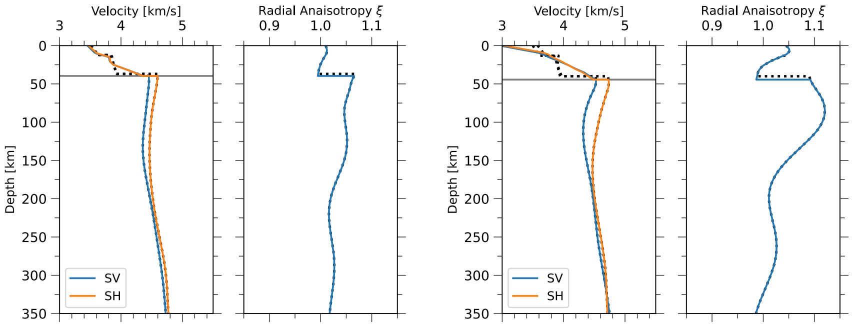
(a) IU.CTAO

(b) G.CAN

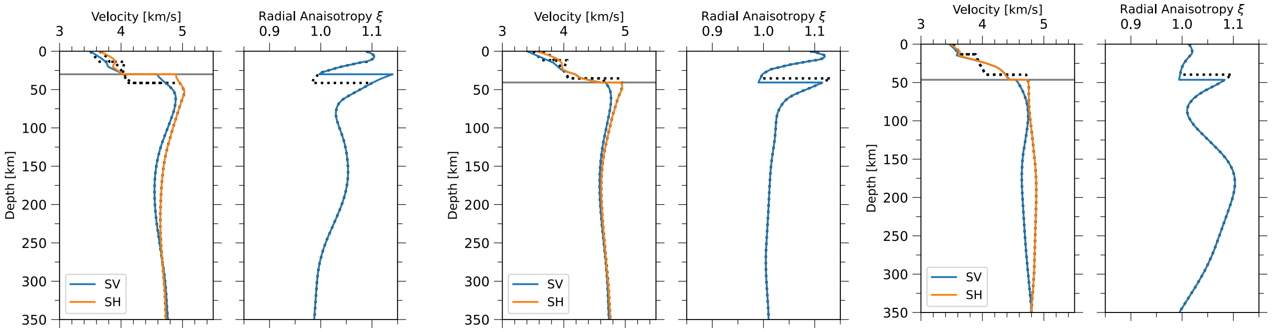
(c) IU.MBWA

(d) IU.NWAO

(e) II.WRAB

Figure S6: Local reference structural models (SV and SH velocities and radial anisotropy) for each station. Solid colored lines represent the reference SV and SH wave models used in this study taken from the 3-D radially anisotropic tomographic model (Yoshizawa, 2014), replacing the crust with AuSREM (Kennett et al., 2013; Salmon et al., 2013) and AusMoho (Kennett et al., 2011, 2023).

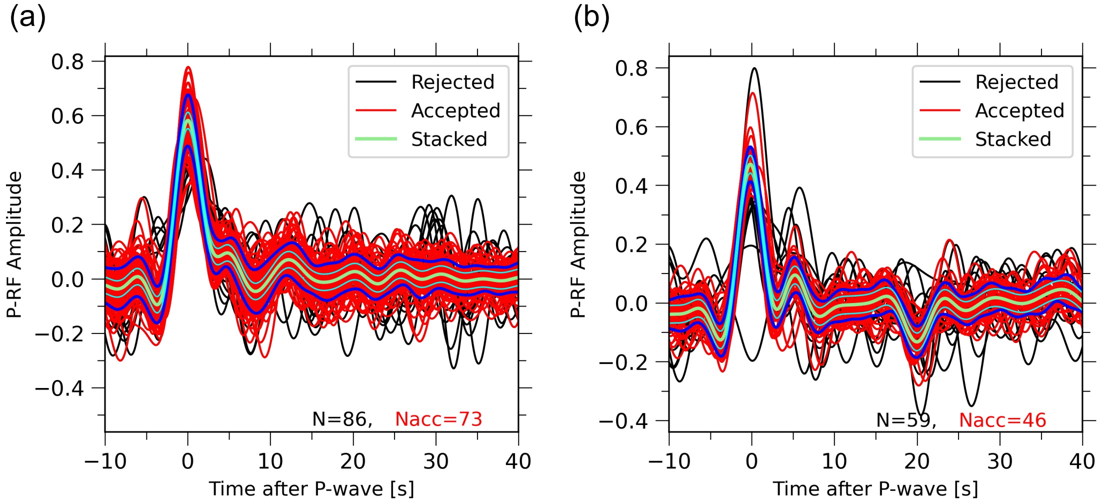

Figure S7: Same as Figure 2 (b, c) in the main text, but with the addition of uncertainty estimates. The thick blue line shows the standard deviation calculated from the accepted RF traces, while the thin cyan lines indicate the typical uncertain range (± 0.03) inferred from the inversion process.

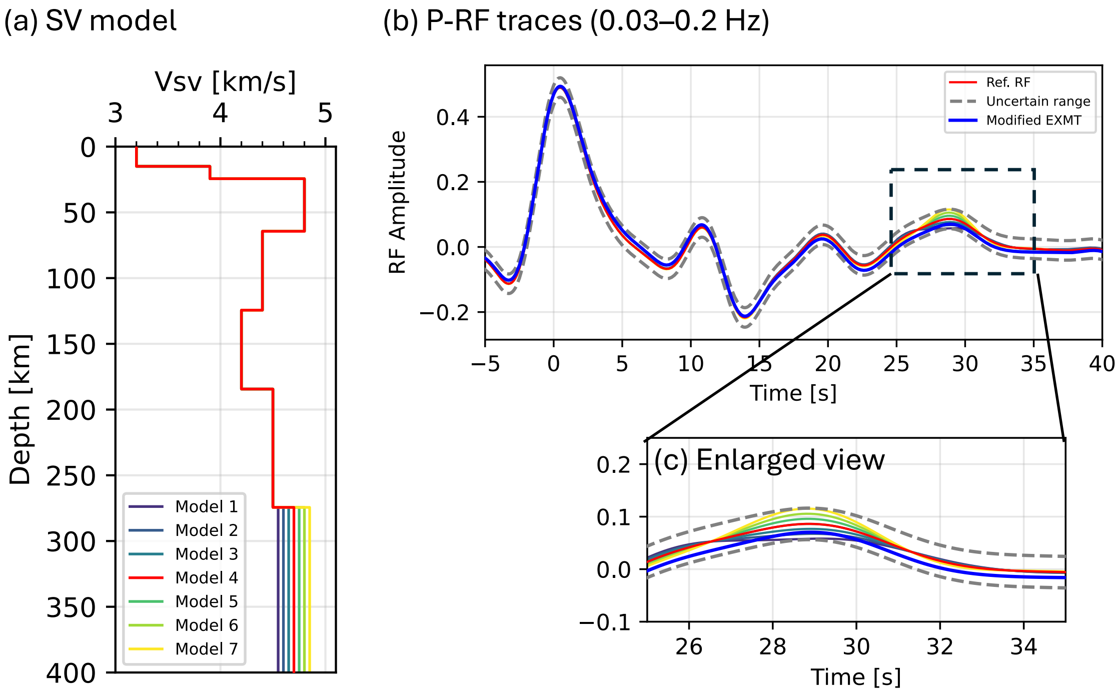

Figure S8: Assessment of uncertainties arising from different RF processing methods for synthetic data. (a) 7 SV-velocity models used to synthesize P-RFs shown in panel (b). (b) P-RF traces filtered between 0.03–0.2 Hz. The red line is the reference RF calculated from the SV velocity model #4 (red line in (a)) using the water-level (WL) deconvolution method. The blue line shows the RF trace from the same model, but processed using the modified EXMT method used for observed data in this study. The other colored lines represent P-RFs (with WL) for the other SV models, with colors corresponding to the model numbers in (a). Gray dashed lines indicate the uncertain range (± 0.03), which is a typical value inferred from the Bayesian inversion. (c) Enlarged view of the dashed black rectangle in (b), highlighting amplitude differences near 30 s.

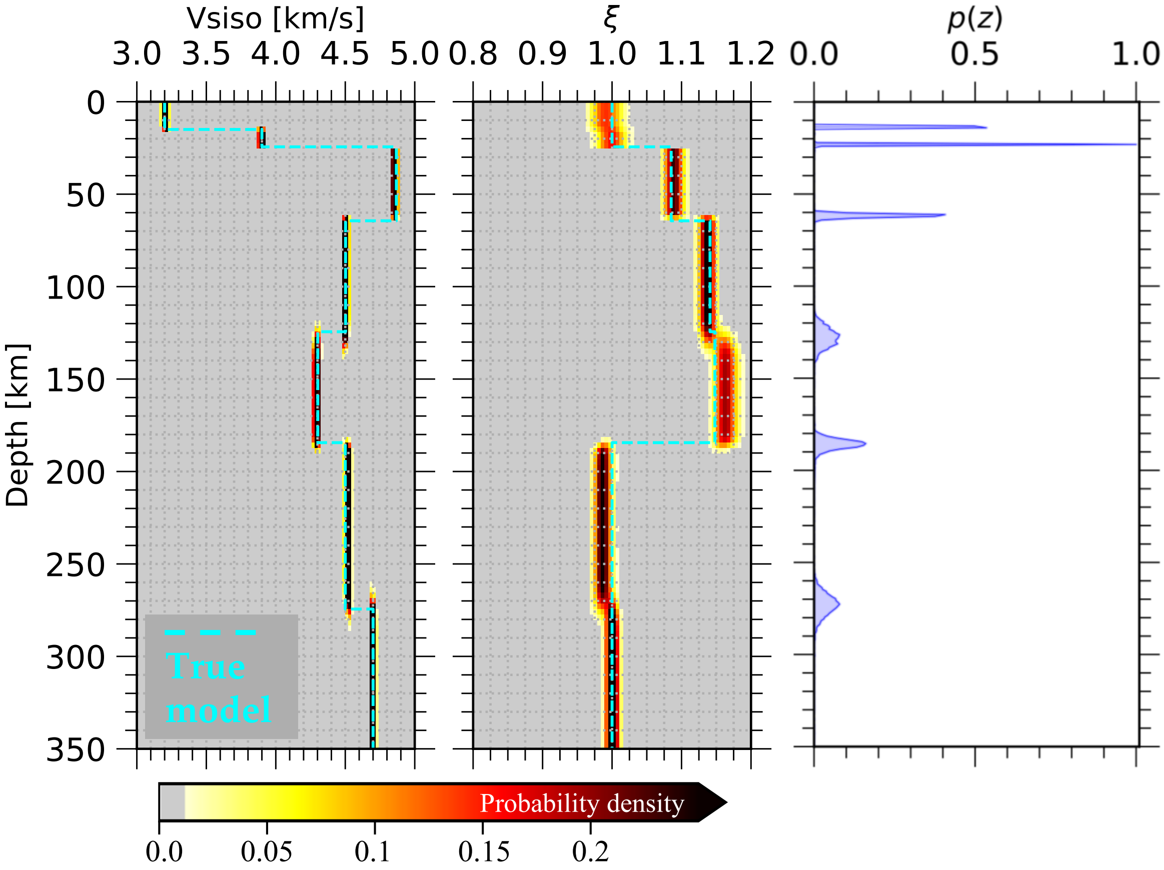

Figure S9: Recovery test using synthetic RFs generated with the multi-taper spectral estimation method, treated as input (observed) data. Posterior distributions of isotropic S-wave velocity (left), radial anisotropy (middle), and discontinuity depths (right). Cyan dashed lines in the left and middle panels represent the true model used to generate the synthetic data.

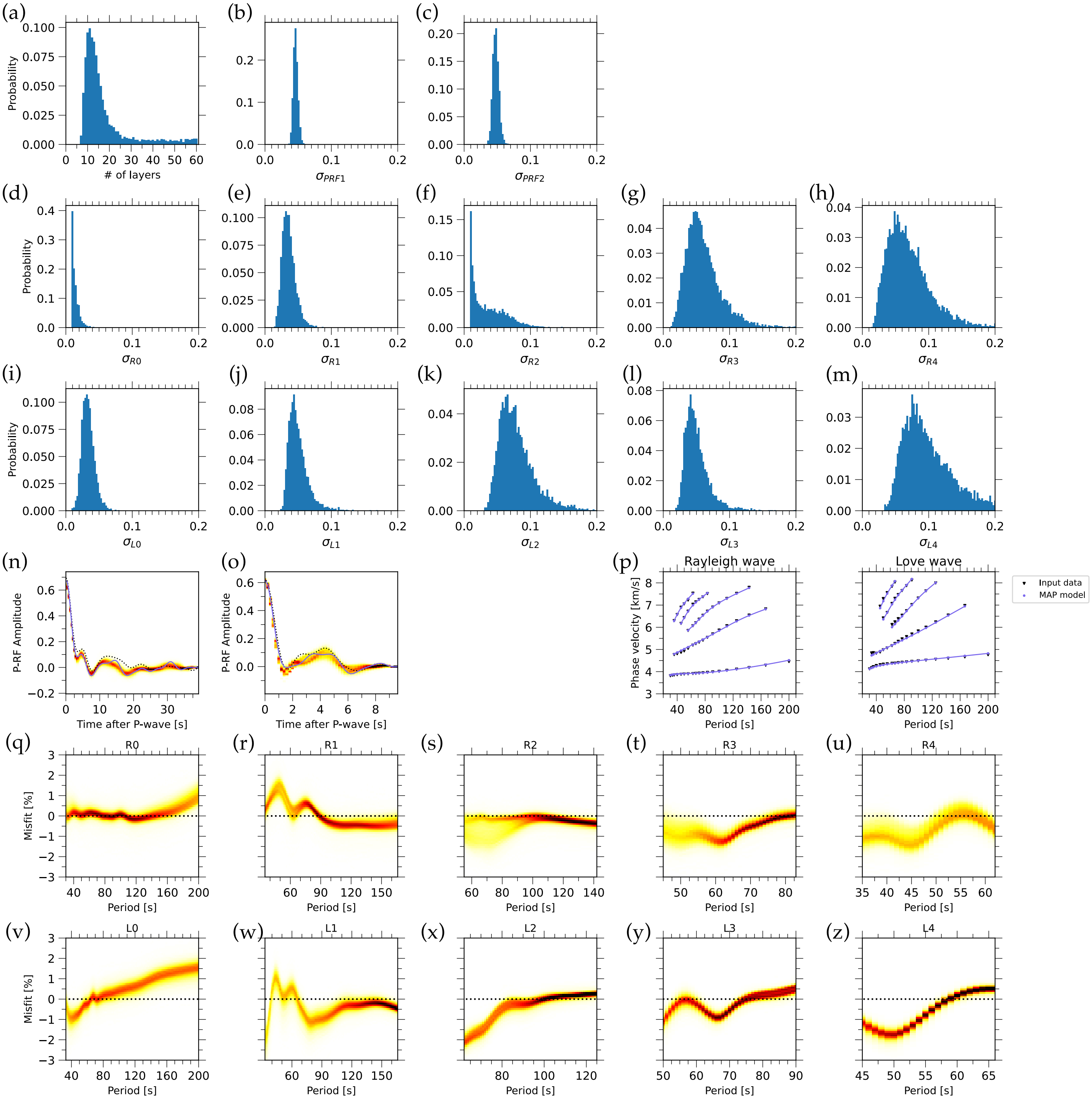

Figure S10: Posterior distributions of hyperparameters and marginal distributions of data misfit for IU.CTAO results using the eastern event group (Figure 5 (b)). (a) The number of layers. (b, c) Data noises for the low-frequency P-RF (σ_{PRF1}) and the high-frequency P-RF (σ_{PRF2}). Data noises for each mode of (d-h) Rayleigh and (i-m) Love waves. R0 and L0 indicate the fundamental-mode Rayleigh and Love waves, and Rx and Lx ($1 \leq x \leq 4$) represent their overtones. (n, o) Marginal posteriors of misfit distribution of (n) low- and (o) high-frequency P-RFs. Black dotted lines and purple solid lines indicate the objective data to be fitted in the inversion process and best-fitted P-RF traces. (p) The best-fitted dispersion curves for Rayleigh and Love waves. Purple lines and dots represent the best-fit synthetic data. Black inverse triangles show the dispersion data from phase speed maps (Yoshizawa, 2014). Marginal misfit distributions between the objective and predicted dispersion curves for (q-u) Rayleigh and (v-z) Love waves. The misfit values are shown in the form of fractional perturbation, $\frac{c_{pre}-c_{obs}}{c_{pre}} \times 100$, following Taira and Yoshizawa (2020). Notations of Rx and Lx are the same as (d-m). Black dotted lines represent the zero-misfit.

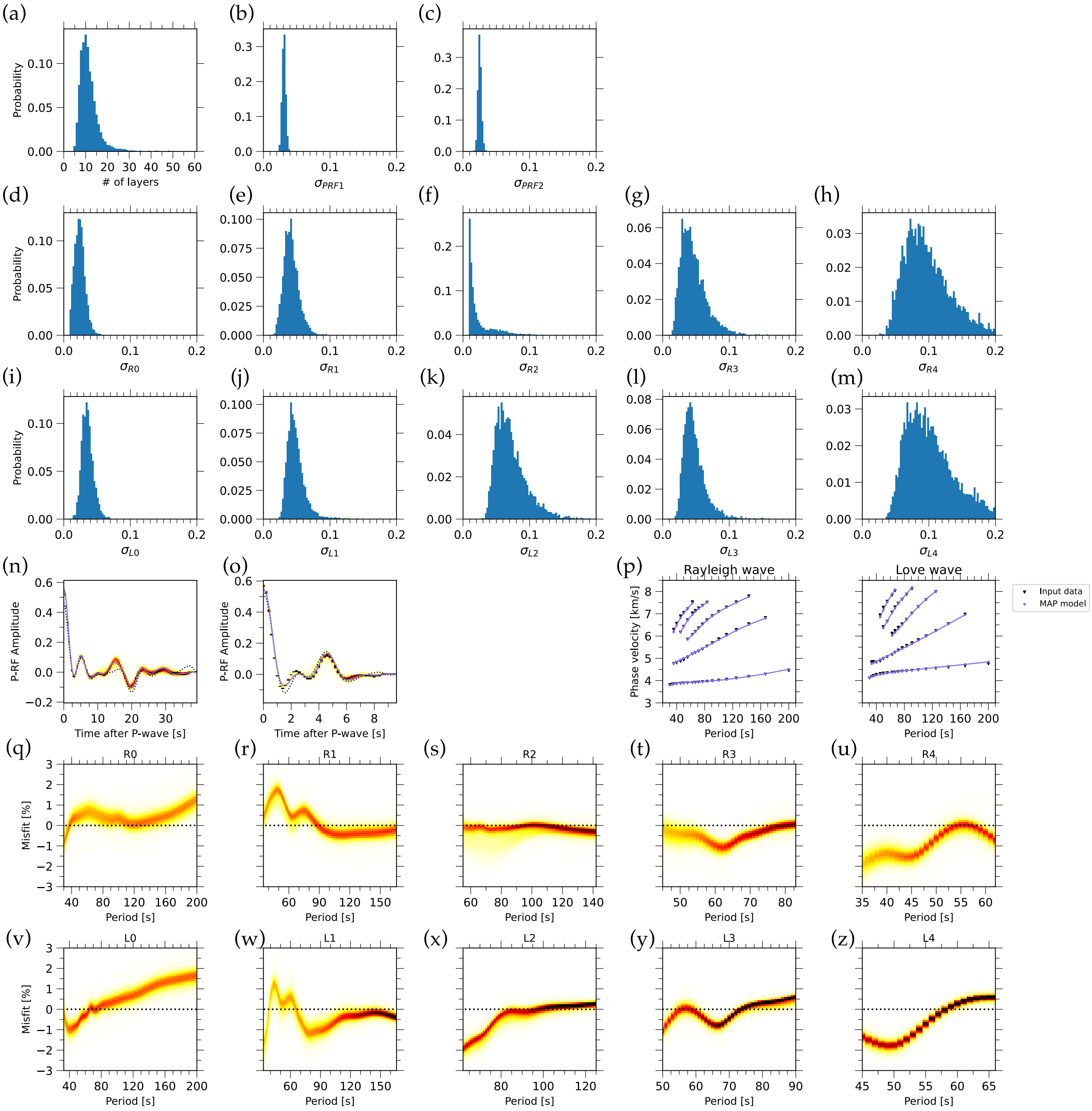

Figure S11: Same as Figure S7, but for the western event group (Figure 5 (c) in the main text).

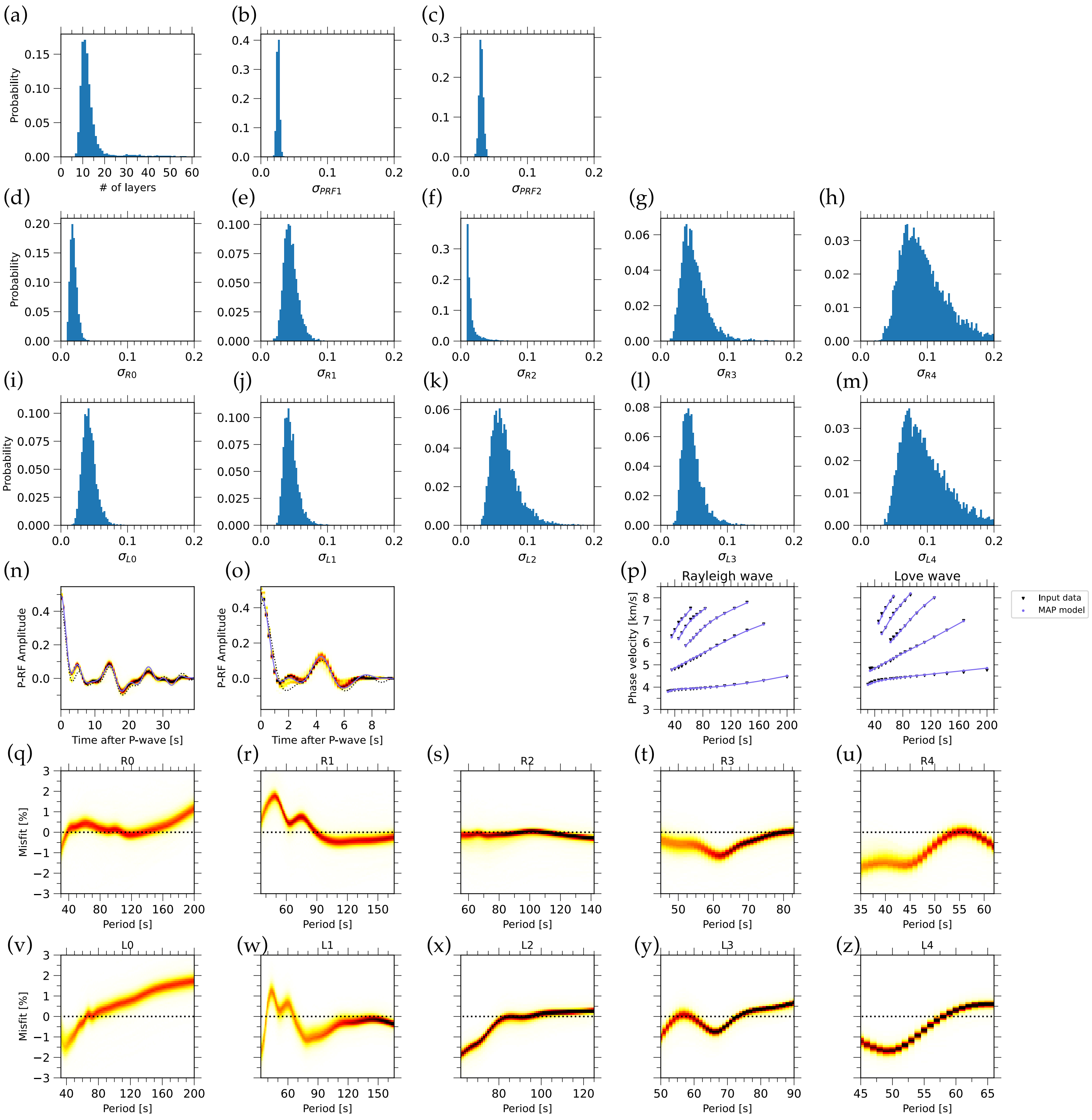

Figure S12: Same as Figure S7, but for the northern event group (Figure 5 (d) in the main text).

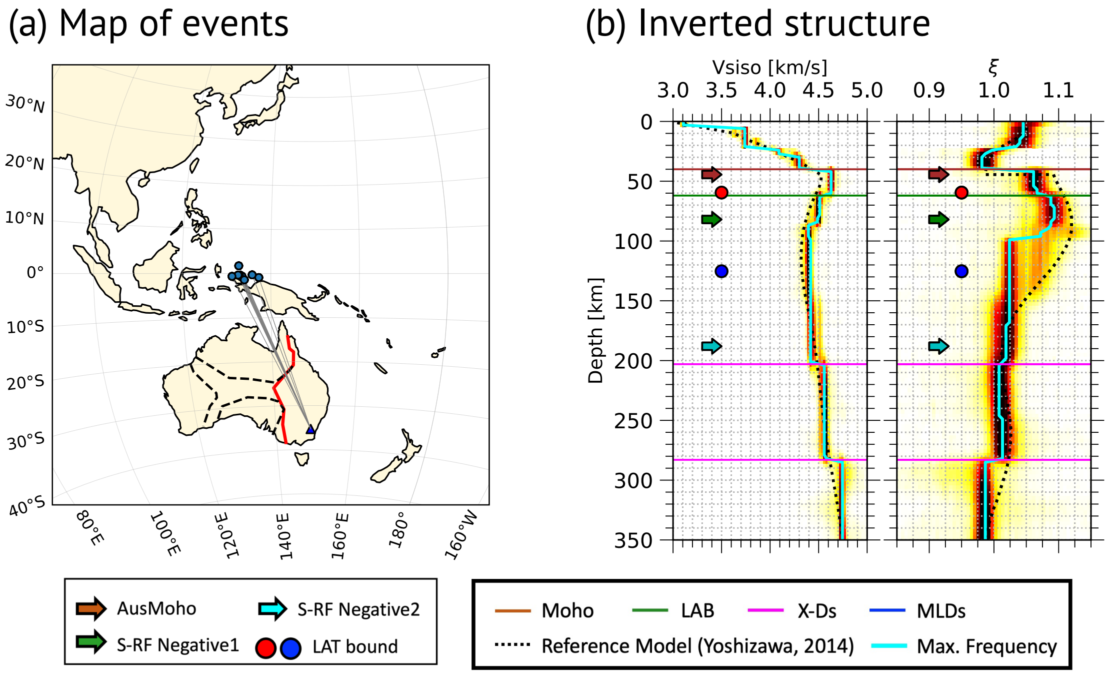

Figure S13: Same as Figure 6 in the main text, but with an additional inversion result for CAN, showing a shear-wave velocity drop at 65 km depth.

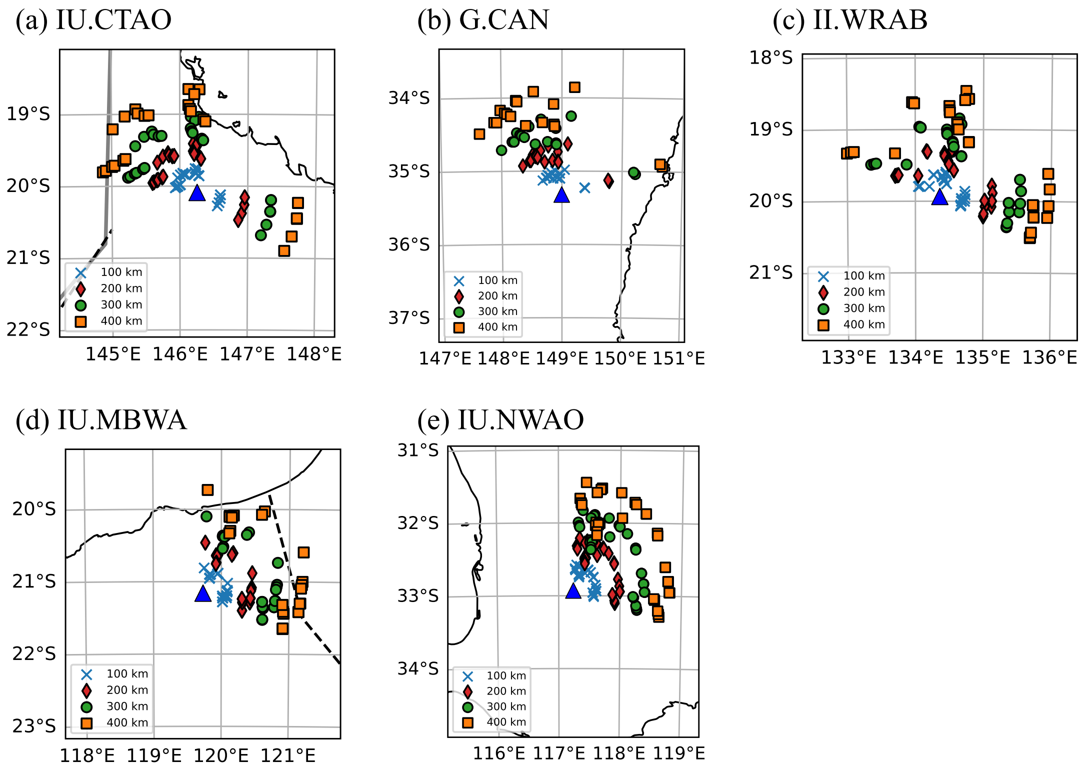

Figure S14: The piercing point maps for Ps phases at five employed stations: (a) G.CAN, (b) IU.CTAO, (c) II.WRAB, (d) IU.MBWA, and (e) IU.NWAO. The colored symbols indicate the piercing points at four distinctive depths, 100km, 200km, 300km, and 400km, with legends in each figure. These piercing points are calculated for the averaged slowness and back-azimuth corresponding to the stacked P-RF dataset used in this study.

Table S1: Standard deviation of the random perturbations for each model parameter in the MCMC proposal.

Interface depths $\boldsymbol{z}$	4 km
Standard deviations for SWDs and P-RFs $\boldsymbol{\sigma}$	0.01
$\boldsymbol{V_{SV}}$ & $\boldsymbol{V_{SH}}$	0.02 km/s

References

Dziewonski, A. M., & Anderson, D. L. (1981). Preliminary reference Earth model. *Physics of the Earth and Planetary Interiors*, *25*(4), 297–356. https://doi.org/10.1016/0031-9201(81)90046-7

Kennett, B. L. N., Salmon, M., Saygin, E., & Group, A. W. (2011). AusMoho: the variation of Moho depth in Australia. *Geophysical Journal International*, *187*(2), 946–958. https://doi.org/10.1111/j.1365-246x.2011.05194.x

Kennett, B. L. N., Fichtner, A., Fishwick, S., & Yoshizawa, K. (2013). Australian Seismological Reference Model (AuSREM): mantle component. *Geophysical Journal International*, *192*(2), 871–887. https://doi.org/10.1093/gji/ggs065

Kennett, B. L. N., Gorbatov, A., Yuan, H., Agrawal, S., Murdie, R., Doublier, M. P., et al. (2023). Refining the Moho across the Australian continent. *Geophysical Journal International*, *233*(3), 1863–1877. https://doi.org/10.1093/gji/ggad035

Salmon, M., Kennett, B. L. N., & Saygin, E. (2013). Australian Seismological Reference Model (AuSREM): crustal component. *Geophysical Journal International*, *192*(1), 190–206. https://doi.org/10.1093/gji/ggs004

Shibutani, T., Ueno, T., & Hirahara, K. (2008). Improvement in the Extended-Time Multitaper Receiver Function Estimation TechniqueShort Note. *Bulletin of the Seismological Society of America*, *98*(2), 812–816. https://doi.org/10.1785/0120070226

Taira, T., & Yoshizawa, K. (2020). Upper-mantle discontinuities beneath Australia from transdimensional Bayesian inversions using multimode surface waves and receiver functions. *Geophysical Journal International*, *223*(3), 2085–2100. https://doi.org/10.1093/gji/ggaa442

Yoshizawa, K. (2014). Radially anisotropic 3-D shear wave structure of the Australian lithosphere and asthenosphere from multi-mode surface waves. *Physics of the Earth and Planetary Interiors*, *235*, 33–48. https://doi.org/10.1016/j.pepi.2014.07.008